Chemical Science

ROYAL SOCIETY OF CHEMISTRY

PERSPECTIVE

View Article Online
View Journal | View Issue

Check for updates

Cite this: *Chem. Sci.*, 2020, **11**, 12233

All publication charges for this article have been paid for by the Royal Society of Chemistry

Received 27th July 2020
Accepted 21st October 2020

DOI: 10.1039/d0sc04100a

rsc.li/chemical-science

Ligand-protected gold/silver superatoms: current status and emerging trends

Haru Hirai,[a] Shun Ito,[a] Shinjiro Takano,[a] Kiichirou Koyasu[ab] and Tatsuya Tsukuda *[ab]

Monolayer-protected gold/silver clusters have attracted much interest as nano-scale building units for novel functional materials owing to their nonbulk-like structures and size-specific properties. They can be viewed as ligand-protected superatoms because their magic stabilities and fundamental properties are well explained in the framework of the jellium model. In the last decade, the number of ligand-protected superatoms with atomically-defined structures has been increasing rapidly thanks to the well-established synthesis and structural determination by X-ray crystallography. This perspective summarizes the current status and emerging trends in synthesis and characterization of superatoms. The topics related to synthesis include (1) development of targeted synthesis based on transformation, (2) enhancement of robustness and synthetic yield for practical applications, and (3) development of controlled fusion and assembly of well-defined superatoms to create new properties. New characterization approaches are also introduced such as (1) mass spectrometry and laser spectroscopies in the gas phase, (2) determination of static and dynamic structures, and (3) computational analysis by machine learning. Finally, future challenges and prospects are discussed for further promotion and development of materials science of superatoms.

1 Introduction

Metal clusters, which are defined as assemblies of several to hundreds of metal atoms, exhibit novel physicochemical properties due to size-specific structures such as nonbulk-like atomic packing and quantized electronic structures.[1–5] Because of these unique features, metal clusters have attracted considerable attention as promising building units of new functional materials. Surface protection by organic ligands enables these clusters to be treated as stable chemical entities. Historically, small gold clusters protected by phosphines (PR_3) and halides (X^-) have been synthesized with atomic precision in the last five decades.[6,7] Their geometric structures have been determined by single-crystal X-ray diffraction (SCXRD) and their

[a]*Department of Chemistry, Graduate School of Science, The University of Tokyo, 7-3-1 Hongo, Bunkyo-ku, Tokyo 113-0033, Japan. E-mail: tsukuda@chem.s.u-tokyo.ac.jp*

[b]*Elements Strategy Initiative for Catalysts and Batteries (ESICB), Kyoto University, Katsura, Kyoto 615-8520, Japan*

Haru Hirai received his B.S. degree in 2018 and M.S. degree in 2020 from The University of Tokyo. He is currently a PhD candidate at the University of Tokyo under the supervision of Prof. Tatsuya Tsukuda. His PhD project is the atomically-precise synthesis and functionalization of ligand-protected gold-based clusters.

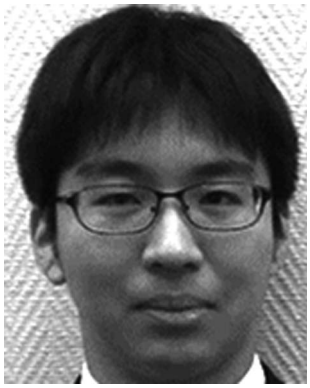

Shun Ito received his B.S. degree in 2019 from The University of Tokyo. He is currently a PhD candidate at the University of Tokyo under the supervision of Prof. Tatsuya Tsukuda. His PhD project is the characterization of ligand-protected metal clusters in the gas phase.

Open Access Article. Published on 21 October 2020. Downloaded on 2/15/2026 11:04:09 AM.
This article is licensed under a Creative Commons Attribution-NonCommercial 3.0 Unported Licence.

Open Access Article. Published on 21 October 2020. Downloaded on 2/15/2026 11:04:09 AM. This article is licensed under a Creative Commons Attribution-NonCommercial 3.0 Unported Licence.

stability has been theoretically explained in terms of electronic structures. The preparation of thiolate (RS^-)-protected Au nanoparticles reported by Brust and Schiffrin in 1994 paved the way for monolayer-protected Au clusters (MPCs) having higher stability than phosphine-protected Au clusters.[8] This perspective summarizes the current understanding of the structural properties of MPCs,[9,10] followed by recent efforts and new trends in the development of atomically-precise nanochemistry.

1.1 Atomically precise synthesis and structural determination

First, the history of the atomically-precise synthesis and structural determination of MPCs is reviewed by highlighting selected benchmark works reported in the last couple of decades. The existence of a series of magic sizes and size-dependent evolution of the electronic structures in MPCs were reported in early works by Whetten and Murray.[11–14] Atomically-precise synthesis of MPCs was established not later than 2010 based on the chemical reduction of precursor Au(I)SR complexes followed by size-focusing treatment and fractionation. Mass spectrometric studies by Tsukuda and Jin identified the currently well-known magic clusters $[Au_{25}(SR)_{18}]^-$, $Au_{38}(SR)_{24}$, and $Au_{144}(SR)_{60}$.[15–17] At present, nearly atomically-precise synthesis up to $Au_{\sim2000}(SC_6H_{13})_{\sim290}$ has been achieved by Dass.[18] After important theoretical predictions of structural features of MPCs by Landman,[12] Garzón,[19] and Häkkinen,[20] the ground-breaking paper by Kornberg in 2007 revealed the formation of $Au(SR)_2$ and $Au_2(SR)_3$ staples on the surface of the Au_{79} core of $Au_{102}(SR)_{44}$.[21] Kornberg's work also highlighted the importance of the SCXRD method for establishing the correlation between structures and properties. Murray and Jin elucidated that $[Au_{25}(SR)_{18}]^-$ and $Au_{38}(SR)_{24}$ have icosahedral Au_{13} and bi-icosahedral Au_{23} cores, respectively, protected by $Au(SR)_2$ and $Au_2(SR)_3$ units.[22–24] The ability of theoretical calculations to predict structures has also been demonstrated. Grönbeck and Aikens respectively predicted the geometric structures of $[Au_{25}(SR)_{18}]^-$ and $Au_{38}(SR)_{24}$ independently of the SCXRD results.[25,26] The structure of $Au_{144}(SR)_{60}$ predicted by Häkkinen[27] was, 10 years later, proved by SCXRD by Wu.[28] In the last decade, the library of MPCs with atomically-defined structures has been expanded remarkably. The organic ligands include phosphines, thiolates, alkynyls ($RC{\equiv}C^-$), and N-heterocyclic carbenes (NHC), and the metal elements include Au, Ag, Cu and their alloys with Pd, Pt, Cd, Hg, and Ir. Fig. 1 plots the number of MPCs whose structures have been determined by SCXRD and clearly shows the rapid expansion of the universe of MPCs.

1.2 Superatom concept

Since the pioneering works on Al clusters by Castleman, Khanna, and Jena,[29–32] the "superatom concept" has been successfully applied to explain the magic stabilities, electronic structures and chemical properties of simple metal clusters in gas phase.[4,5,33–36] The jellium model[37] qualitatively describes the behavior of valence electrons confined within the clusters of coinage metals (Cu, Ag, Au) having a single valence electron in the *n*s atomic orbitals ($n = 4, 5, 6$).[38] The spherical jellium model

Shinjiro Takano received his PhD degree in 2016 from The University of Tokyo under the supervision of Prof. Tatsuya Tsukuda. After working as a postdoctoral researcher at the Department of Chemistry, The University of Tokyo for two years, he was promoted to Assistant Professor at the same department in 2018. His research interests are mainly the investigation of the fundamental properties of chemically modified Au clusters through the development of novel atomically-precise synthetic approaches.

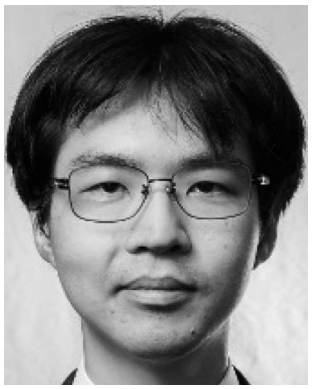

Kiichirou Koyasu received a PhD degree in 2006 from Keio University under the supervision of Prof. Atsushi Nakajima. After postdoctoral research at the University of Konstanz, Germany and Nagoya University, Japan, he became Research Associate at Keio University in 2009, and then moved to Tohoku University six months later. In 2013 he was promoted to an Associate Professor at The University of Tokyo. His research interests include the exploration and characterization of metal-based clusters in the gas phase.

Tatsuya Tsukuda received a PhD degree in 1994 from The University of Tokyo under the supervision of Prof. Tamotsu Kondow. After postdoctoral research at RIKEN, he was appointed Assistant Professor at The University of Tokyo in 1994, and in 2000 he became an Associate Professor at the Institute for Molecular Science. He was promoted to Professor at the Catalysis Research Center of Hokkaido University in 2007, before moving to The University of Tokyo in 2011. His research interests cover the atomically-precise synthesis and characterization of gold clusters protected by ligands and their catalytic applications.

 This journal is © The Royal Society of Chemistry 2020

Open Access Article. Published on 21 October 2020. Downloaded on 2/15/2026 11:04:09 AM.
This article is licensed under a Creative Commons Attribution-NonCommercial 3.0 Unported Licence.

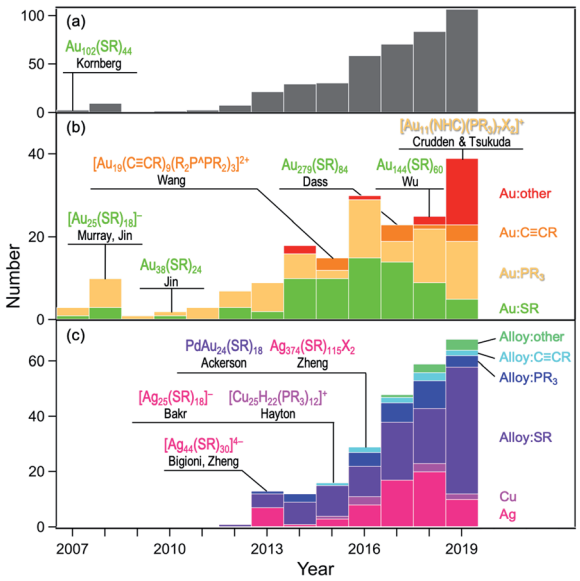

Fig. 1 Annual numbers of crystals data of (a) coinage-metal MPCs, (b) Au MPCs, and (c) Ag/Cu/alloy MPCs deposited in the Cambridge Crystallographic Data Centre since 2007, with selected benchmark studies.

assumes that individual metal atoms delocalize the valence electrons over a uniformly charged spherical volume. Such confinement of the electrons leads to the quantized superatomic orbitals (SOs) labeled 1S, 1P, 1D, 2S, 1F, 2P, 1G, …. The electronic shells of coinage metal clusters are closed when the total number of valence electrons is 2, 8, 18, 20, 34, 40, 58, …. Spherical coinage metal clusters can be viewed as superatoms, given that the electronic shell structures are formed as in the case of conventional atoms. Häkkinen extended this concept to MPCs by introducing a simple counting scheme for the formal number of valence electrons (n^*) in MPCs $[M_xL_y]^z$:[39,40]

$$n^* = Ax + By - z \quad (1)$$

where A and B represent the number of valence electrons supplied from an individual M atom and ligand L, respectively.

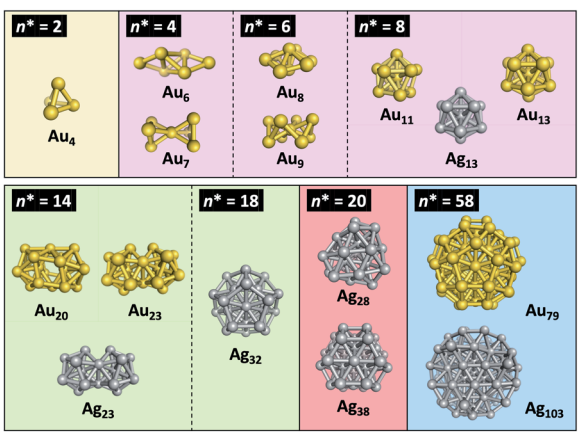

Fig. 2 Superatomic Au/Ag cores identified by SCXRD.

A is 2, 1, 0, and −1 for Cd/Hg, Ag/Au, Pd/Pt, and Rh/Ir, respectively. B takes 0 for phosphines and carbenes, whereas it takes −1 for halides, thiolates, selenolates, and alkynyls because of their electron-withdrawing nature. Fig. 2 shows the icosahedral and decahedral **(Au/Ag)X**(n*e) cores found in representative Au/Ag MPCs: $\mathbf{Au_4}$(2e), $\mathbf{Au_{11}}$(8e), $\mathbf{Au_{13}}$(8e), $\mathbf{Ag_{13}}$(8e), $\mathbf{Ag_{32}}$(18e), $\mathbf{Ag_{28}}$(20e), $\mathbf{Ag_{38}}$(20e), $\mathbf{Au_{79}}$(58e), and $\mathbf{Ag_{103}}$(58e).[41] The n* values of these cores agree with those predicted for spherical superatoms. Therefore, these isolated Au/Ag MPCs with spherical shapes can be viewed as chemically-modified Au/Ag superatoms with closed electronic structures.

The huge impact of structural factors, such as size, shape, and composition, on the electronic structures of superatomic cores can be qualitatively explained within the framework of the spherical and modified jellium model. The origin of important phenomena, such as the closure of electronic shells, evolution of an energy gap between the highest-occupied molecular orbital (HOMO) and the lowest-unoccupied molecular orbital (LUMO), and energy shift of the orbitals upon doping, was qualitatively explained by considering how the volume, shape, and depth of the jellium potential are affected by structural factors. The reduction of the HOMO–LUMO gap with size can be understood by the increase of the volume of the jellium potential and the occupation of SOs in high-energy and dense regions (Fig. 3). When the spherical jellium is deformed, the SOs originally degenerated in energy are split due to the Jahn–Teller effect.[42] For example, the energy shift of the SOs upon deformation into oblate and prolate shapes is schematically shown in Fig. 3. Triply degenerated 1P SOs in the spherical jellium are split into two subgroups in the oblate-shaped jellium: $1P_z$ along the short axis is destabilized compared to $1P_x$ and $1P_y$. As a result, the oblate superatoms with a closed subshell configuration $(1S)^2(1P)^4$ become stable, as can be found in $\mathbf{Au_8}$(6e) and $\mathbf{Au_9}$(6e) (Fig. 2). In contrast, the prolate superatoms with closed subshell configurations such as $(1S)^2(1P)^2$ and $(1S)^2(1P)^6(1D)^6$ become stable, as can be seen in $\mathbf{Au_6}$(4e), $\mathbf{Au_7}$(4e), $\mathbf{Au_{20}}$(14e), $\mathbf{Au_{23}}$(14e), and $\mathbf{Ag_{23}}$(14e) (Fig. 2). The effects

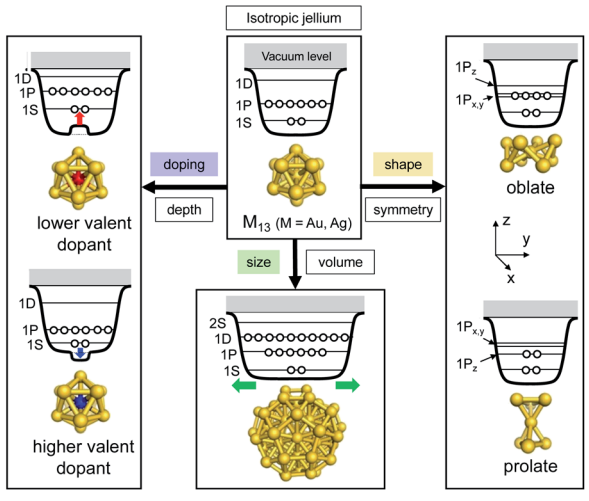

Fig. 3 Schematic representation of effects of size, shape and doping on jellium potentials.

Open Access Article. Published on 21 October 2020. Downloaded on 2/15/2026 11:04:09 AM. This article is licensed under a Creative Commons Attribution-NonCommercial 3.0 Unported Licence.

of doping on the electronic structures of superatoms can be qualitatively predicted by a two-step spherical jellium model,[43–45] which is based on the idea that the host and dopant atoms provide different but uniform background potential. When the dopant atom has higher valency than the host atoms, the SOs are stabilized because the effective potential become more attractive, and *vice versa* (Fig. 3). The energy ordering of SOs can be changed by doping. For example, if the higher-valence dopant is introduced at the center of a spherical superatom, the S and P SOs having density at the center are stabilized more than the D and F SOs having several nodal planes at the center. As a result, the energy ordering of the SOs is changed to 1S, 1P, 2S, 1D, 2P, 1F, … so that the shell closing occurs at $n^* = 2$, 8, 10, 20, 26, 40, …. Although such structural simplification smears out the detailed structural information obtained by SCXRD, these qualitative pictures provide a rational design principle for the development of new functionalized superatoms. However, there are a class of MPCs that fall outside the scope of the superatom concept. For example, the n^* values of face-centered cubic (fcc) Au cores of $Au_{8n+4}(SR)_{4n+8}$ cannot be explained by the simple jellium model,[46] but by the grand unified model (GUM).[47] In the GUM, the Au cores are viewed as assemblies of smaller superatomic units, such as triangular **Au$_3$**(2e) and tetrahedral **Au$_4$**(2e). In this perspective, we will focus only on the MPCs that can be viewed as chemically-modified Au/Ag superatoms.

1.3 Aim of this perspective

The rapid growth of materials chemistry of chemically-modified superatoms in the last decade has been made possible by the establishment of atomically-precise synthesis and structural determination by SCXRD. Thanks to reproducible synthesis, a wide variety of fundamental properties such as optical and photophysical properties, catalysis, and magnetic properties has been studied by diverse researchers with different backgrounds and interests.[48] These studies have demonstrated that chemically-modified superatoms are promising building units of functional materials in the future. In addition, if we could establish a periodic table of the superatoms as artificial elements on a nanoscale, it would create a new paradigm of nanoscience.

However, several problems must be overcome for the further development of materials chemistry of superatoms. First, most of the new superatoms have been obtained serendipitously because the formation of superatoms is based on stochastic processes of the aggregation of metal atoms and ligands, and because there is no guarantee that single crystals will be obtained. Thus the synthesis and crystallization of superatoms rely on the carpet-bombing approach of screening the synthetic conditions such as precursor materials, solvents, reducing agents, and reaction temperature. It is necessary to increase the chance of unexpected discoveries and ultimately to establish the targeted synthesis of desired superatoms. Secondly, the stability and scale of the synthesized quantity of superatoms must be increased for future applications. Thirdly, a strategy for creating new properties and functions by taking advantage of cooperative interaction between individual superatoms is needed. In addition to these challenges related to synthesis, new characterization methods which are supplementary to SCXRD are required. For example, the characterization of superatoms isolated in vacuum would provide information of inherent structures and stabilities of the superatoms without the interference from the solvents and counterions. Experimental tools to probe the dynamic aspects of superatoms are also required. This perspective summarizes recent progress toward overcoming the challenges for synthesis and developing new characterization methods.

2 Emerging trends in synthesis

2.1 Targeted synthesis by transformation

This section explains the transformations of a preformed atomically-precise superatom into another superatom with different size, composition, and structure. Synthesis through such transformation has advantages in terms of selectivity and targetability over the conventional methods based on stochastic aggregation of metal atoms and ligands. In addition, such transformations may produce novel products that cannot be obtained by conventional methods. In the following, the transformation processes are categorized into two types: addition and exchange reactions.

2.1.1 Addition reactions. Takano and Tsukuda recently developed an efficient bottom-up method using $[MAu_8(TPP)_8]^{n+}$ (TPP = PPh_3; $n = 3$ for M = Au; $n = 2$ for M = Pd, Pt) as starting materials.[49–53] The growth and doping reactions were initiated by doping a hydride (H^-) to the central, unligated M atom of the **M@Au$_8$**(6e) core by the reaction with $NaBH_4$ (Fig. 4a). The resulting hydride-doped **HM@Au$_8$**(8e) superatom has a closed electronic structure with eight electrons, but is reactive toward nucleophilic attack to AuCl(TPP) because a high-lying, occupied 1P superatomic orbital is sterically exposed. The **HAu@Au$_8$**(8e) superatom underwent selective growth to the well-known **Au@Au$_{10}$**(8e) superatom *via* stepwise incorporation of two Au(I)Cl units and release of a proton (Fig. 4b).[49] The number of Au atoms introduced is determined by the steric hinderance exerted on incoming Au(I)Cl caused by the pre-existing TPP ligands. In contrast, novel, hydrogen-containing bi- and trimetallic superatoms **HPd@Z$_2$Au$_8$**(8e) (Z = Cu, Ag, or Au) were synthesized *via* regioselective doping of two Z(I)Cl units to **HPd@Au$_8$**(8e) (Fig. 4c).[50,52] The reaction of **HM@Au$_8$**(8e) (M = Pd, Pt) with Au(I)-SR (SR = primary thiolate) oligomers yielded the previously known clusters $[MAu_{24}(SR)_{18}]^0$ (Fig. 4d) with a high efficiency (yield > 50%, 50–200 mg), whereas a new cluster, $[PdAu_{23}(SR')_{17}]^0$ having an unprecedented, hexagonal close-packed **Pd@Au$_{12}$**(6e) core, was obtained when SR′ was a secondary thiolate.[53] The **HM@Au$_8$**(8e) clusters (M = Pd, Pt) were efficiently transformed into $[MAu_{24}(C{\equiv}CR)_{18}]^{2-}$ upon the addition of a stoichiometric amount of Au(I)–C≡CR oligomers (Fig. 4d).[53]

Larger superatoms can be obtained by the controlled growth of "seed" superatoms. Xie achieved selective growth of $[Au_{25}(p\text{-MBA})_{18}]^-$ (p-MBA = 4-SC_6H_4COOH) to $Au_{38}(p\text{-MBA})_{24}$ and further to $[Au_{44}(p\text{-MBA})_{26}]^{2-}$ by kinetically controlled reduction

 This journal is © The Royal Society of Chemistry 2020

Open Access Article. Published on 21 October 2020. Downloaded on 2/15/2026 11:04:09 AM.
This article is licensed under a Creative Commons Attribution-NonCommercial 3.0 Unported Licence.

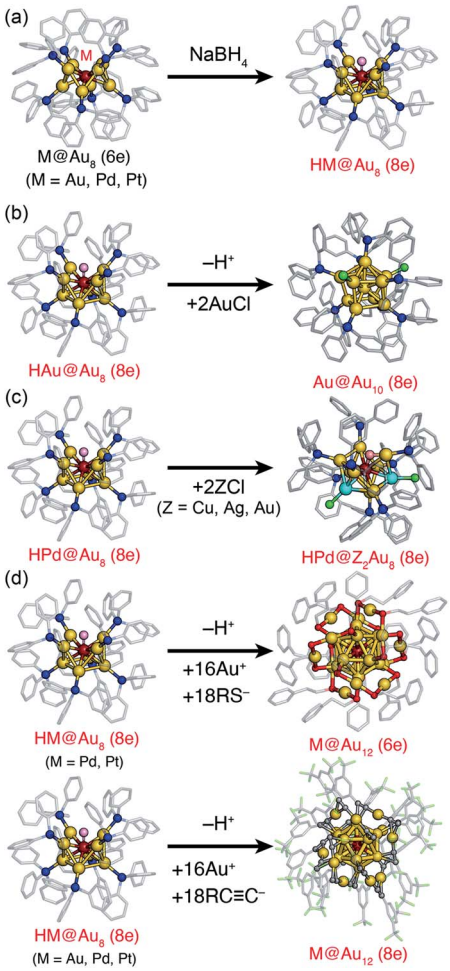

Fig. 4 (a) Hydride doping to **M@Au$_8$**(6e) (M = Au, Pd, Pt) to form **HM@Au$_8$**(8e). (b) Growth, (c) doping, (d) chemical modification of **HM@Au$_8$**(8e). Color code: yellow = Au; wine red = Pd or Pt; cyan = Cu, Ag, or Au; pink = H; red = S; green = Cl; blue = P; gray = C. Organic residues are depicted as sticks.

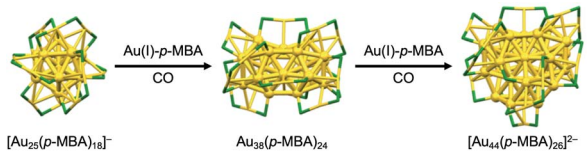

Fig. 5 Controlled growth of thiolate-protected Au superatoms. Color code: yellow = Au; green = S. Organic residues are omitted for simplicity.

of Au(I)-*p*-MBA oligomers by carbon monoxide (CO) in the presence of $[Au_{25}(p\text{-MBA})_{18}]^-$ (Fig. 5).[54] Two growth mechanisms operate in slow reduction with CO; (1) the LaMer-like growth pathway, in which particles monotonically get larger with the addition of newly reduced Au(I)-*p*-MBA oligomers and (2) the aggregative growth pathway, in which two particle agglomerate to form a larger particle.

2.1.2 Exchange reactions. Doping of heteroatoms to Au/Ag superatoms has been conventionally conducted by co-reduction of dopant ions with Au/Ag(I) precursors. Recently, more efficient and controllable routes based on galvanic/antigalvanic reactions have been developed.[55–58] Coinage metals (Cu, Ag, Au) and group 12 metals (Cd and Hg) from the complexes have been successfully introduced into pre-synthesized Au/Ag superatoms by replacing the constituent atoms. NMR spectroscopy showed that the Cd or Hg dopant is introduced to the surface of the Au_{13} core,[59] while SCXRD demonstrated that the Au dopant prefers the center of the Ag core.[60,61] These results suggested that the location of the dopant is not determined by the metal exchange process, but by the intrinsic stability of the bimetallic clusters. Surprisingly, Pradeep discovered that the metal exchange takes place between $[Au_{25}(PET)_{18}]^-$ (PET = PhC_2H_4S) and $[Ag_{25}(2,4\text{-DMBT})_{18}]^-$ (2,4-DMBT = $2,4\text{-}(CH_3)_2C_6H_3S$) in their physical mixture.[62] The Au/Ag composition was controlled over a wide range simply by the mixing ratio of the clusters. It was proposed that this intercluster metal exchange may proceed *via* a dimerized intermediate, $[Au_{25}Ag_{25}(PET)_{18}(2,4\text{-DMBT})_{18}]^{2-}$.[63] Tsukuda found that $[PtAu_{24}(PET)_{18}]^-$ with an open-shell **Pt@Au$_{12}$**(7e) core was obtained stoichiometrically by electron transfer from $[PtAu_{24}(PET)_{18}]^{2-}$ to $[PtAu_{24}(PET)_{18}]^0$ in their physical mixture.[64]

Ligand exchange of preformed superatoms is a versatile strategy to tune their properties while retaining the core structures. For example, the thermal stabilities of **Au$_{11}$**(8e) and **Au$_{13}$**(8e) are enhanced by replacing phosphine with NHC[65] and thiolate with selenolate,[66,67] respectively. In contrast, when introducing thiolates having significantly different steric hinderance, the size and/or atomic packing of the superatomic cores can be modulated. Table 1 shows examples of the ligand-exchange-induced size/structure transformation (LEIST)[68–81] observed for thiolate-protected Au/Ag superatoms. The fact that the products depend on the thiolates used indicates that interligand interaction due to steric hinderance of the tail groups of the ligands plays a crucial role. Reversible LEIST was observed as listed in Table 2. **Au$_{20}$**(8e) superatomic cores of $Au_{28}(TBBT)_{20}$ (TBBT = $4\text{-}(CH_3)_3CC_6H_4S$) and $Au_{28}(c\text{-HT})_{20}$ (*c*-HT = $c\text{-}C_6H_{11}S$) exhibit different catalysis for CO oxidation due to differences in geometric structures.[79] ESI-MS analysis by Bakr demonstrated that conversion from $[Ag_{25}(2,4\text{-DMBT})_{18}]^-$ to $[Ag_{44}(4\text{-FTP})_{30}]^{4-}$ (4-FTP = $4\text{-}FC_6H_4S$) proceeded *via* dimerization, while reverse conversion proceeded by dissociative disproportionation to form $[Ag_{25}(2,4\text{-DMBT})_{18}]^-$ and smaller Ag(I)-SR fragments.[80] These examples illustrated that LEIST allows us to access new clusters that cannot be synthesized by the direct reduction method, although it is difficult to predict what type of transformation will be induced by ligand exchange.

2.2 Improving robustness

In principle, superatoms are stabilized against aggregation by protection with the organic ligands. However, in practice, most of the superatoms lack long-term stability under ambient conditions and decompose under harsh conditions. Therefore, improvement of the robustness is an essential requirement for practical applications.

One of the promising methods for protecting Au superatoms recently found is to use N-heterocyclic carbenes (NHCs) which

Open Access Article. Published on 21 October 2020. Downloaded on 2/15/2026 11:04:09 AM. This article is licensed under a Creative Commons Attribution-NonCommercial 3.0 Unported Licence.

Table 1 Examples of irreversible LEIST

Precursors		Products		
Composition[a]	Core	Composition[a]	Core	Ref.
$[Au_{25}(PET)_{18}]^-$	**Au_{13}**(8e)	$Au_{20}(TBBT)_{16}$	**Au_7**(4e)	70
		$Au_{28}(TBBT)_{20}$	**Au_{14}**(8e)	71
$Au_{38}(PET)_{24}$	**Au_{23}**(14e)	$Au_{36}(TBBT)_{24}$	**Au_{28}**(12e)	72
		$Au_{30}(StBu)_{18}$	**Au_{22}**(12e)	73
$Au_{144}(PET)_{60}$	**Au_{114}**(84e)	$Au_{133}(TBBT)_{52}$	**Au_{107}**(81e)	74 and 75
		$Au_{99}(SPh)_{42}$	—[b]	76
$[Ag_{59}(2,5\text{-}DCBT)_{32}]^{3-}$	—[b]	$[Ag_{25}(2,4\text{-}DMBT)_{18}]^-$	**Ag_{13}**(8e)	77
		$[Ag_{29}(1,3\text{-}BDT)_{12}(PPh_3)_4]^{3-}$	**Ag_{13}**(8e)	77
		$[Ag_{44}(SR)_{30}]^{4-}$, SR = 2,4-DCBT/4-FTP/4-CTP	**Ag_{32}**(18e)	77

[a] PET = PhC_2H_4S; TBBT = 4-$(CH_3)_3CC_6H_4S$; 2,5-DCBT = 2,5-$Cl_2C_6H_3S$; 2,4-DMBT = 2,4-$(CH_3)_2C_6H_3S$; 1,3-BDT = 1,3-$C_6H_4S_2$; 2,4-DCBT = 2,4-$Cl_2C_6H_3S$; 4-FTP = 4-FC_6H_4S; 4-CTP = 4-ClC_6H_4S. [b] Unknown.

Table 2 Examples of reversible LEIST

Composition[a]	Core	Composition[a]	Core	Ref.
$Au_{30}(StBu)_{18}$	**Au_{20}**(12e)	$Au_{36}(SR)_{24}$, SR = SPh/TBBT	**Au_{24}**(12e)	78
$Au_{28}(TBBT)_{20}$	**Au_{20}**(8e)	$Au_{28}(cHT)_{20}$	**Au_{20}**(8e)	79
$[Ag_{25}(2,4\text{-}DMBT)_{18}]^-$	**Ag_{13}**(8e)	$[Ag_{44}(4\text{-}FTP)_{30}]^{4-}$	**Ag_{32}**(18e)	80
$[PtAg_{28}(SAdm)_{18}(PPh_3)_4]^{2+}$	**$PtAg_{12}$**(8e)	$[PtAg_{28}(cHT)_{18}(PPh_3)_4]^{2+}$	**$PtAg_{12}$**(8e)	81

[a] TBBT = 4-$(CH_3)_3CC_6H_4S$; *c*HT = *c*-$C_6H_{11}S$; 2,4-DMBT = 2,4-$(CH_3)_2C_6H_3S$; 4-FTP = 4-FC_6H_4S; SAdm = $C_{10}H_{16}S$.

are known to form highly robust self-assembled monolayers on Au(111) surfaces.[82–84] The first NHC-protected Au superatom reported was **Au_{11}**(8e) in $[Au_{11}(NHC^{iPr})(TPP)_7Cl_2]^+$ (NHC^{iPr} = $C_7H_4N_2(CH(CH_3)_2)_2$) synthesized by exchanging a phosphine ligand of $[Au_{11}(TPP)_8Cl_2]^+$ with NHC^{iPr}.[65] A single NHC^{iPr} ligand selectively replaced the TPP ligand located between two Cl ligands to yield $[Au_{11}(NHC^{iPr})(TPP)_7Cl_2]^+$ (Fig. 6a). $[Au_{11}(NHC^{iPr})(TPP)_7Cl_2]^+$ showed much higher thermal stability than $[Au_{11}(TPP)_8Cl_2]^+$ and acted as an electrocatalyst for CO_2 reduction. The high stability was ascribed to a strong Au–C bonding based on the collision-induced dissociation (CID) MS and theoretical calculation.[65,85] Following the above report, Au superatoms protected only by other NHCs and halogens have been reported.[86–88] For example, $[Au_{13}(NHC^{Bn})_9Cl_3]^{2+}$ (NHC^{Bn} = $C_7H_4N_2(CH_2Ph)_2$) (Fig. 6b)[86] and $[Au_{13}(di\text{-}NHC)_5Br_2]^{3+}$ (di-NHC = $PhCH_2\text{-}C_7H_4N_2\text{-}(CH_2)_3\text{-}C_7H_4N_2\text{-}CH_2Ph$) (Fig. 6c)[88] with an icosahedral **Au_{13}**(8e) core were synthesized. The latter was robust at temperatures (−70 °C and 100 °C) and under various redox and pH conditions (pH = 1–11) and survived for <6 min even when treated with aqua regia. SCXRD analysis suggested that the ligand layers of NHCs rigidified the **Au_{13}**(8e) core by the CH–π and π–π interaction between the adjacent NHC ligands. As a result, $[Au_{13}(NHC^{Np})_9Cl_3]^{2+}$ (NHC^{Np} = $C_7H_4N_2(CH_2(2\text{-}C_{10}H_7))_2$) and $[Au_{13}(di\text{-}NHC)_5Br_2]^{3+}$ exhibit visible photoluminescence with quantum yields as high as 16 and 15%, respectively.[86,88]

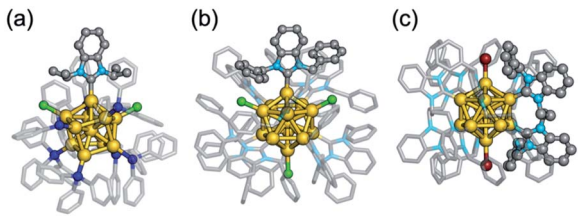

Fig. 6 Structures of ultrarobust Au superatoms protected by N-heterocyclic carbenes. (a) $[Au_{11}(NHC^{iPr})(TPP)_7Cl_2]^+$, (b) $[Au_{13}(NHC^{Bn})_9Cl_3]^{2+}$, (c) $[Au_{13}(di\text{-}NHC)_5Br_2]^{3+}$. Color code: yellow = Au; gray = C; sky blue = N; blue = P; light green = Cl; dark red = Br. Organic residues are depicted as sticks.

2.3 Scaling up yields

Another challenge for synthesis is to scale up the yield. Typical yields of lab-scale synthesis are on the order of a few milligrams owing to the stochastic nature of the cluster formation and to the loss during rigorous purification. Such low yield limits the characterization methods that can be applied and the scope of practical applications.

The most impressive examples are >100 g synthesis of $[Ag_{44}(p\text{-}MBA)_{30}]^{4-}$ (Fig. 7a) and >10 g synthesis of $[Ag_{44}(3,4\text{-}DFBT)_{30}]^{4-}$ (3,4-DFBT = 3,4-$F_2C_6H_3S$) having a common **Ag_{32}**(18e) superatomic core.[89,90] The reason for the large-scale synthesis of $[Ag_{44}(SR)_{30}]^{4-}$ is the high yield (>95%) due to extraordinarily high stability: the HOMO–LUMO gap is as large as 0.78 eV and the coordinating solvents as well as the ligands are involved in the protection. Paste-base synthesis in the solid state was also reported as a greener (less wasteful) method.[91] Hitherto-known bimetallic clusters $[MAu_8(TPP)_8](NO_3)_2$ (M =

 This journal is © The Royal Society of Chemistry 2020

Open Access Article. Published on 21 October 2020. Downloaded on 2/15/2026 11:04:09 AM. This article is licensed under a Creative Commons Attribution-NonCommercial 3.0 Unported Licence.

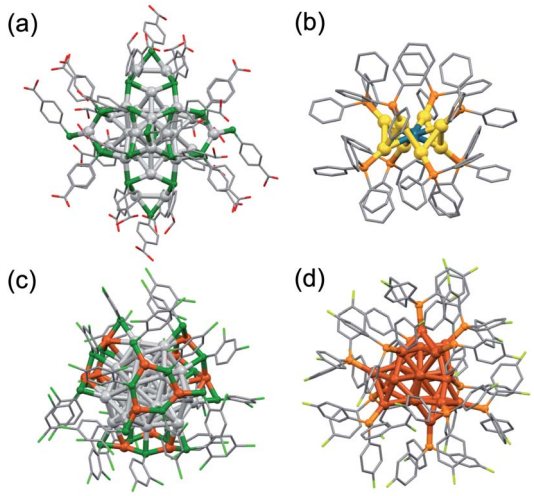

Fig. 7 Structures of clusters synthesized on a large scale: (a) $[Ag_{44}(p\text{-}MBA)_{30}]^{4-}$, (b) $[PdAu_8(TPP)_8]^{2+}$, (c) $[Ag_{28}Cu_{12}(2,4\text{-}DCBT)_{24}]^{4-}$, (d) $[Cu_{25}H_{22}(4\text{-}FPP)_{12}]^{+}$. Color code: yellow = Au; light gray = Ag; brown = Cu; dark blue = Pd; green = S; orange = P; gray = C; red = O; light green = Cl; light yellow = F. Organic residues are depicted as sticks.

Pd, Pt) were selectively synthesized on a large scale (0.2–1 g) by co-reduction of $Au(NO_3)(TPP)$ and $M(TPP)_4$ in a one-pot reaction (Fig. 7b).[50,53] Tsukuda successfully obtained $MAu_{24}(SR)_{18}$ on a large scale (50–200 mg) by using $[MAu_8(TPP)_8](NO_3)_2$ as starting materials of conversion (see Section 2.1.1).[53] Zheng reported gram-scale synthesis of $[Ag_{28}Cu_{12}(2,4\text{-}DCBT)_{24}]^{4-}$ (2,4-DCBT = 2,4-$Cl_2C_6H_3S$) with the **Ag_{28}**(20e) superatomic core (Fig. 7c).[92] Zhu synthesized $[Cu_{25}H_{22}(4\text{-}FPP)_{12}]^{+}$ (4-FPP = P(4-$FC_6H_4)_3$) in gram-scale *via* a high-yield (83%) route under aerobic conditions (Fig. 7d).[93] The yield is much higher than that of $[Cu_{25}H_{22}(TPP)_{12}]^{+}$ under inert conditions (*ca.* 150 mg, 23%) because 4-FPP is more electron-withdrawing than TPP. The large-scale syntheses outlined above are based on high selectivity due to the intrinsic stability of the products and careful control of the reaction kinetics. However, it is not trivial to scale up the yield while retaining the selectivity by simply increasing the concentration and/or volume of the precursor solutions in the batch synthesis. A possible solution is to use fluidic systems as demonstrated in the synthesis of organic,[94] inorganic,[95] and nano-materials.[96] In contrast to the conventional batch mixing, microfluidic system allows to scale up the quantity of the MPCs while retaining their quality (size distribution) because it provides efficient and homogeneous mixing conditions of solutions regardless of the total volumes of the solutions. Microfluidic synthesis of superatoms will be one of the interesting challenges for synthesis in the future.

2.4 Bonding and assembly of superatoms

An increasing number of new molecules and materials have been created on the basis of systematic understanding of fundamental properties and bonding interaction of individual elements. Thus, it is an interesting challenge to create a hierarchical world on a nanoscale using superatoms as artificial elements, similar to conventional molecular chemistry. This section examines recent progress in the development of quasi-molecules of superatoms (superatomic molecules) and higher assemblies of superatoms.

2.4.1 Superatomic molecules. According to the super valence bond theory developed by Yang and Cheng,[97] some prolate superatoms can be viewed as superatomic molecules in terms of electronic structures (Fig. 8a). For example, the prolate superatoms **Au_{20}**(14e) and **Au_{23}**(14e) can be viewed as dimers of open-shell **Au_{11}**(7e) and **Au_{13}**(7e) superatoms linked by sharing an edge $(Au^{+})_2$ or facet $(Au^{+})_3$, respectively.[97] Density functional theory (DFT) calculations on **Au_{20}**(14e) and **Au_{23}**(14e) show that their electron configuration is expressed as $(1\sigma_s)^2(1\sigma_s^*)^2(1\pi_{p_x,p_y})^4(1\sigma_{p_z})^2(1\pi_{p_x,p_y}^*)^4$,[97] indicating that the formal bond order between the Au_{11} and Au_{13} units is one. Namely, the bonding scheme in **Au_{20}**(14e) and **Au_{23}**(14e) is similar to that of the F_2 molecule. Similarly, bi-icosahedral **Ag_{23}**(14e) and **Au_{25}**(14e) cores correspond to the facet-shared dimer of **Ag_{13}**(7e) and vertex-shared dimer of **Au_{13}**(7e), respectively.[98,99] Bi-, tri-, and penta-icosahedral superatoms **Au_{25}**(16e), **Au_{37}**(24e), and **Au_{60}**(40e) are constructed by closed-shell **Au_{13}**(8e) and correspond to a dimer, trimer, and pentamer of the rare gas atoms, respectively.[87,100–105] Bimetallic superatomic molecules **Pt_2Ag_{33}**(16e) and **Pt_3Ag_{44}**(22e) contain icosahedral units of **$PtAg_{12}$**(8e): their bonding schemes are analogues to those of dimers of rare gas atoms and tri-halogen anions, respectively.[106] The **Au_{22}**(22e) core in $[Au_{22}(Ph_2P(CH_2)_8PPh_2)_6]^0$ corresponds to a homodimer of **Au_{11}**(11e)[107] which are bonded by a 1D≡1D triple bond, similarly to transition metal binuclear complexes.[108]

These examples imply that a class of quasi-molecules can be developed by bonding various superatomic units through

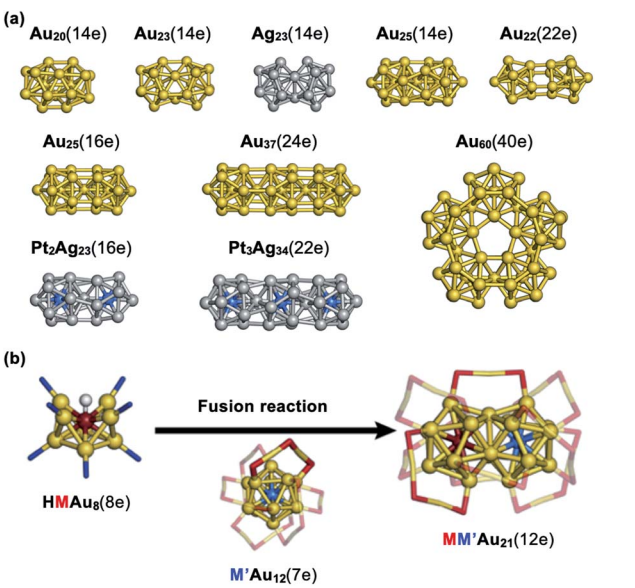

Fig. 8 (a) Examples of homo-superatomic molecules. Color code: yellow = Au; light gray = Ag; light blue = Pt. (b) Targeted synthesis of superatomic molecules by fusion. Color code: yellow = Au; wine red = Pd or Pt; blue = P; red = S; white = H. Au–S oligomers and organic residues are omitted for simplicity.

Open Access Article. Published on 21 October 2020. Downloaded on 2/15/2026 11:04:09 AM. This article is licensed under a Creative Commons Attribution-NonCommercial 3.0 Unported Licence.

various bonding schemes. However, their synthesis relies on serendipity; targeted synthesis using well-defined superatoms as precursors is highly demanded for a deeper understanding of the bonding theory of superatoms. Recently, Maran reported the formation of $Au_{38}(SR)_{24}$ by dimerization of $[Au_{25}(SR)_{18}]^0$ (R = C_3H_7, C_4H_9, C_8H_{17}, C_2H_2Ph). This reaction is formally described as:[109]

$$\mathbf{Au_{13}}(7e) + \mathbf{Au_{13}}(7e) \rightarrow \mathbf{Au_{23}}(14e) + (Au^+)_3 \quad (2)$$

The faster reaction with smaller thiolates suggests that the overlap of superatomic orbitals is crucial. Takano and Tsukuda synthesized $\mathbf{MM'Au_{21}}(12e)$ (M, M′ = Pd, Pt) by the reaction between hydride-doped $[HMAu_8(TPP)_8]^+$ and monoanionic $[M'Au_{24}(PET)_{18}]^-$ (Fig. 8b).[110] SCXRD revealed that $\mathbf{MM'Au_{21}}(12e)$ corresponds to homo- and hetero-dimers of $\mathbf{M@Au_{12}}(6e)$ and $\mathbf{M'@Au_{12}}(6e)$. This is the first example of targeted synthesis of hetero-dimers of superatoms *via* fusion reactions of the corresponding precursors. A rare example of hetero-superatomic molecules can be found in $[Au_{20}(H)_3(TPP)_{14}]^{3+}$; the $\mathbf{Au_{20}}(14e)$ core corresponds to a heterodimer of $\mathbf{Au_9}(6e)$ and $\mathbf{Au_{11}}(8e)$ connected *via* two triangular faces.[111]

2.4.2 Superatomic assemblies. The creation of one-, two-, and three-dimensional (1–3D) assemblies of superatomic units has been extensively studied.[112] The methods include direct connection of superatoms *via* metal–metal bonds, bridging the superatoms by ligands, and assembling the superatoms *via* interligand interactions, such as hydrogen bonding, π–π interaction, and CH–Cl interaction. The assemblies of superatoms often show unique and superior properties depending on the nature of the interaction and structures of the assembled structures such as distance and symmetry.[112]

1D assemblies have attracted interest as nanoscale electrical conductors. Maran reported the formation of linear polymers of $[Au_{25}(S_nBu)_{18}]^0$ in the crystal connected by intercluster aurophilic interaction (Fig. 9a).[113] The polymer of the paramagnetic $\mathbf{Au_{13}}(7e)$ units was silent in electron paramagnetic resonance (EPR) measurement because unpaired electrons of neighboring clusters coupled with each other. This electron pairing indicates that the conduction band is fully occupied while the valence band is empty. Theoretical calculation predicted that the polymer of $[Au_{25}(S_nBu)_{18}]^0$ has a band gap of ~0.12 eV at 0 K and shows semiconducting behavior at room temperature. $(AuAg)_{34}(C{\equiv}CAdm)_{20}$ (Adm = $C_{10}H_{16}$) also formed a 1D polymer linked *via* Ag–Au–Ag bonds (Fig. 9b).[114] The conductivity along the polymer chain (1.49×10^{-5} S m^{-1}) was 1800 times higher than that along the interchain direction. The conductivity of the $(AuAg)_{34}$ polymer is 1–3 orders of magnitude higher than that of a 1D polymer of $\mathbf{Au_{15}}(8e)$ linked by weak interligand interactions.[115] The comparison suggests that direct connection by metal–metal bonds promotes the electron transfer.

A super-structure of Ag superatoms with higher dimension has been reported. Zang assembled $Ag_{14}(DT\text{-}o\text{-}C)_6$ (DT-*o*-C = $B_{10}H_{10}C_2S_2$) having $\mathbf{Ag_6}(2e)$ superatomic cores using bidentate pyridyl ligands: the assembly forms 1–3D structures depending on the length of linkers (Fig. 10).[116] The 3D assembly showed extraordinarily high thermal stability and temperature-dependent photoluminescence, which is different from that of monomer. Recently, a 3D assembly of $[AuAg_{21}(SAdm)_{12}]^{3+}$ was produced *via* Ag–F–Ag bonds with SbF_6^- anions.[117] The assembly was enantiopure because of the chiral arrangement of the ligand layer and exhibited circularly polarized luminescence. Red emission was observed in the presence of protic solvents such as methanol, ethanol, and water, but turned off after evaporation of the solvents. There is great scope for developing new functionalized materials by controlling the assembling behaviors of superatoms (*e.g.*, the distance, symmetry, dimensionality and degree of electronic coupling) by appropriately designing the surface modification.

3 Emerging trends in characterization

Ligand-protected Au/Ag superatoms have been characterized by various experimental methods conventionally used in chemical analysis. The methods include SCXRD, mass spectrometry (MS), X-ray photoelectron spectroscopy (XPS), nuclear magnetic

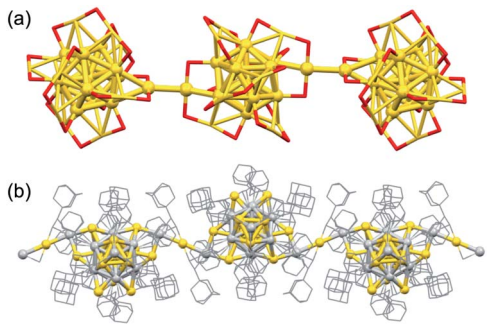

Fig. 9 SCXRD structures of polymers of (a) $[Au_{25}(S_nBu)_{18}]^0$ and (b) $(AuAg)_{34}(C{\equiv}CAdm)_{20}$. Color code: yellow = Au; light gray = Ag; red = S; gray = C. Au–S oligomers and organic residues are depicted as sticks.

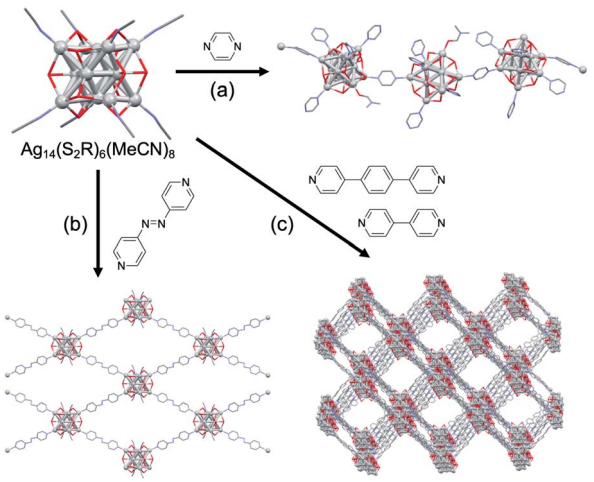

Fig. 10 (a) 1D, (b) 2D, and (c) 3D assembly of $\mathbf{Ag_6}(2e)$ superatoms. Color code: light gray = Ag; red = S; blue = N; gray = C. Organic residues are depicted as sticks.

 This journal is © The Royal Society of Chemistry 2020

Open Access Article. Published on 21 October 2020. Downloaded on 2/15/2026 11:04:09 AM.
This article is licensed under a Creative Commons Attribution-NonCommercial 3.0 Unported Licence.

resonance (NMR), pulse voltammetry, X-ray absorption spectroscopy (XAS), aberration-corrected (scanning) transmission electron microscopy (AC(S)TEM), ultraviolet-visible (UV-visible) optical spectroscopy, Fourier-transform infrared spectroscopy (FT IR), photoluminescence (PL) spectroscopy, and circular-dichroism (CD) spectroscopy. In this section, we focus on emerging trends in experimental characterization and theoretical approach for structural prediction.

3.1 Gas phase methods

Characterization of ligand-protected superatoms isolated in the gas phase provides intrinsic information of superatoms by eliminating perturbations from the surrounding environments (*e.g.* solvent, counterion). Especially when SCXRD is available, correlations between electronic and geometric structures can be established. Electrospray ionization (ESI) is a typical interface to introduce the chemically synthesized superatoms in vacuum in the intact form. After mass selection, the superatoms can be characterized by a variety of gas-phase methods such as collision-induced dissociation (CID) MS, ion mobility (IM) MS, photoelectron spectroscopy (PES), photodissociation (PD) MS, and surface-induced dissociation (SID) MS. We herein limit ourselves to MS, CID MS, and laser spectroscopy. The operating principles of other methods and their application to ligand-protected Au/Ag superatoms can be found in recent publications.[118–122]

3.1.1 Mass spectrometry. The most fundamental application of mass spectrometry is the determination of chemical compositions and net charge of chemically synthesized superatoms. The reaction mechanism for complex processes in solution can be monitored at the molecular level by mass spectrometric detection of the short-lived species involved. Tsukuda detected $[HAu_9(TPP)_8]^{2+}$ and $[HPdAu_8(TPP)_8]^{+}$ having hydrogen-containing superatomic cores **HAu$_9$**(8e) and **HPdAu$_8$**(8e) in the reaction of $[Au_9(TPP)_8]^{3+}$ and $[PdAu_8(TPP)_8]^{2+}$ with $NaBH_4$, respectively.[49,50] Time-resolved ESI MS showed the sequential growth of $[HAu_9(TPP)_8]^{2+}$ to the well-known undecagold cluster $[Au_{11}(TPP)_8Cl_2]^{+}$ by reaction with Au(I)Cl-TPP while releasing the proton.[49] In contrast, hydrogen remained throughout the corresponding growth of $[HPdAu_8(TPP)_8]^{+}$ to unprecedented $[HPdAu_{10}(TPP)_8Cl_2]^{+}$ (Fig. 11a).[50] *In situ* ESI MS has been applied to a variety of solution processes including reductive synthesis,[123,124] seed-mediated growth,[54] and alloying processes of Au/Ag superatoms.[61,63] Xie probed the formation processes of $[Au_{25}(p\text{-MBA})_{18}]^{-}$ (Fig. 11b) to establish total synthesis in the field of nanoscience (*i.e.* synthesis of nanomaterials with atomic precision and by known step-by-step reactions).[124] They detected $[Au(p\text{-MBA})_2]^{-}$ as a by-product and achieved selective synthesis of $[Au_{25}(p\text{-MBA})_{18}]^{-}$ using the stoichiometric amount of $NaBH_4$ Pradeep conducted *in situ* ESI MS of metal-exchange reactions between superatoms.[63] The formation of dimeric species $[Ag_{25}Au_{25}(2,4\text{-DMBT})_{18}(PET)_{18}]^{2-}$ was observed at the initial stage of alloying reactions between $[Au_{25}(PET)_{18}]^{-}$ and $[Ag_{25}(2,4\text{-DMBT})_{18}]^{-}$ (Fig. 11c).

3.1.2 Collision-induced dissociation mass spectrometry. Collision-induced dissociation is one of the techniques coupled with mass spectrometry, where the ligand-protected superatoms are vibrationally and rotationally activated by the collision with gas molecules and led to the dissociation. CID MS of ligand-protected **Au$_{11}$**(8e) and **Au$_{13}$**(8e) superatoms detected the fragment ions with 8 electrons, indicating the dissociation is governed by the electronic stability of the products.[118] In contrast, it was found that the CID of ligand-protected

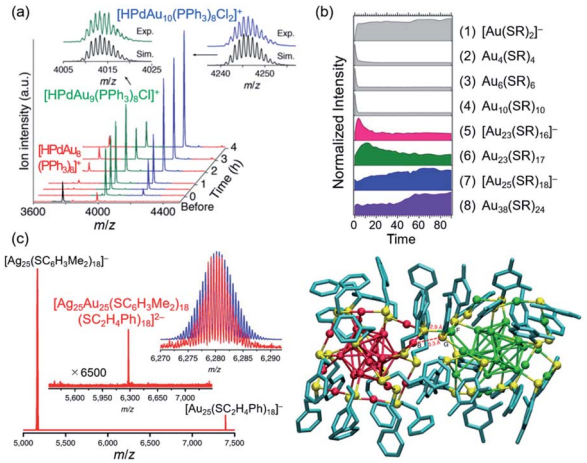

Fig. 11 (a) Time-resolved ESI mass spectra of sequential growth of $[HPdAu_8(TPP)_8]^{+}$ to $[HPdAu_{10}(TPP)_8Cl_2]^{+}$. (b) Time-dependent ESI MS intensity of Au-SR complexes (SR = *p*-MBA) (1–4) and clusters (5–8) during the synthesis of $Au_{25}(SR)_{18}$: (1) $[Au(SR)_2]^{-}$, (2) $Au_4(SR)_4$, (3) $Au_6(SR)_6$, (4) $Au_{10}(SR)_{10}$, (5) $[Au_{23}(SR)_{16}]^{-}$, (6) $Au_{23}(SR)_{17}$, (7) $[Au_{25}(SR)_{18}]^{-}$, (8) $Au_{38}(SR)_{24}$. (c) ESI mass spectrum of the mixture of $[Au_{25}(PET)_{18}]^{-}$ and $[Ag_{25}(2,4\text{-DMBT})_{18}]^{-}$ and DFT-optimized structure of $[Ag_{25}Au_{25}(2,4\text{-DMBT})_{18}(PET)_{18}]^{2-}$. Color code: red = Au; green = Ag; yellow = S; blue = C. Adapted with permission from ref. 50, 124 and 63. Copyright 2018 American Chemistry Society, copyright 2018 American Chemistry Society, and copyright 2016 Nature Publishing Group.

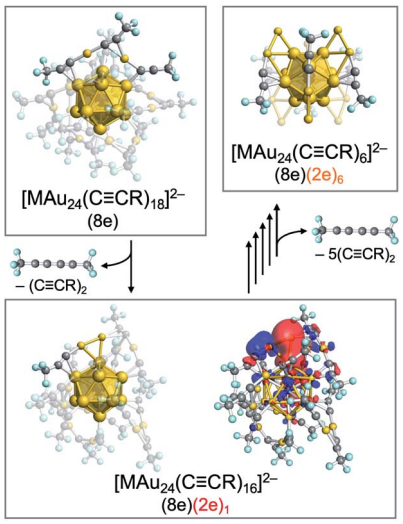

Fig. 12 Scheme of the formation of superatomic assemblies *via* CID of 1,3-diyne from $[MAu_{24}(C{\equiv}CR)_{18}]^{2-}$. Color code: yellow = Au; gray = C; light blue = F.

Open Access Article. Published on 21 October 2020. Downloaded on 2/15/2026 11:04:09 AM.
This article is licensed under a Creative Commons Attribution-NonCommercial 3.0 Unported Licence.

superatoms can induce reductive elimination of ligands. Pradeep found that CID of $[Ag_{18}(TPP)_{10}H_{16}]^{2+}$ resulted in the reductive elimination of H_2 and the formation of $\mathbf{Ag_{17}H_{14}}^{+}$(2e) and $\mathbf{Ag_{17}}^{+}$(16e).[125] Tsukuda showed that the CID of $[MAu_{24}(C{\equiv}CR)_{18}]^{2-}$ (M = Pd, Pt; R = 3,5-$(CF_3)_2C_6H_3$) having an icosahedral $\mathbf{M@Au_{12}}$(8e) superatomic core mainly afforded $[MAu_{24}(C{\equiv}CR)_{18-2n}]^{2-}$ (n = 1–6) having (8 + 2n) electrons *via* sequential reductive elimination of 1,3-diynes RC≡C–C≡CR (Fig. 12).[126] Theoretical calculations on a model system $[MAu_{24}(C{\equiv}CCF_3)_{16}]^{2-}$ predicted that the increased electrons are not accommodated in a 1D superatomic orbital distributed over the cluster, but are localized at the $Au_2(C{\equiv}CCF_3)_1$ sites formed from the original $Au_2(C{\equiv}CCF_3)_3$ motif by desorption of $CF_3C{\equiv}C{-}C{\equiv}CCF_3$. Thus, $[MAu_{24}(C{\equiv}CR)_{18-2n}]^{2-}$ can be viewed as novel assemblies of superatoms with 8e and 2e (Fig. 12). The desorption step of 1,3-diynes continued to n = 6, leading to the formation of $M@Au_{12}[Au_2(C{\equiv}CR)_1]_6$. These results demonstrate the ability of CID MS to explore novel superatoms that cannot be synthesized by the conventional thermal processes. These partially naked Au superatoms produced *via* hyperthermal CID processes can be tested as new catalysts if they are collected by a proper method such as deposition on solid or powder surface.

3.1.3 Laser-based spectroscopies. Since the first report by Tsukuda in 2017,[127] the adiabatic electron affinities (AEAs) of $[Au_{25}(SC_6H_{13})_{18}]^0$, $[Au_{25}(PET)_{18}]^0$, and $[Ag_{25}(2,4\text{-DMBT})_{18}]^0$ were determined by PES to be 2.2, 2.36 ± 0.01, and 2.02 ± 0.01 eV, respectively.[128] These results suggest that the electronic structure of the $\mathbf{M_{13}}$(8e) superatom is not seriously affected by the thiolates and M (M = Ag, Au). In contrast, PES on $[Ag_{25}(2,4\text{-DMBT})_{18}]^-$ and $[MAg_{24}(2,4\text{-DMBT})_{18}]^{2-}$ (M = Pd, Pt) revealed a remarkable doping effect: the electron binding energy of the Ag_{13} core is significantly reduced by replacing the central Ag^+ atom with a Pt or Pd atom (Fig. 13a).[129] The higher-energy shift of the SOs was ascribed to the weaker binding of valence electrons in $M@(Ag^+)_{12}$ (M = Pd, Pt) compared to that in $Ag^+@(Ag^+)_{12}$ due to the reduction in formal charge of the core potential (Fig. 3) and the upward shift of the apparent vacuum level by the presence of a repulsive Coulomb barrier (RCB) for $M@(Ag^+)_{12}$ (Fig. 13b). PES and theoretical calculation on $[Ag_{44}(3,4\text{-DFBT})_{30}]^{4-}$ (3,4-DFBT = 3,4-$F_2C_6H_3S$) by Tsukuda and Häkkinen revealed that AEA of $[Ag_{44}(3,4\text{-DFBT})_{30}]^{3-}$ was negative (Fig. 13c),[130] indicating that electron detachment from $[Ag_{44}(3,4\text{-DFBT})_{30}]^{4-}$ to form $[Ag_{44}(3,4\text{-DFBT})_{30}]^{3-}$ is energetically feasible. However, the tetra-anion is observed to be stable in the gas phase against electron autodetachment even under CID conditions. This observation was explained by the energy barrier associated with the electron detachment due mainly to the RCB being much larger than that for fragmentation (Fig. 13d). Veenstra demonstrated by pump–probe PES on $[Ag_{29}(1,3\text{-BDT})_{12}]^{3-}$ (1,3-BDT = 1,3-$C_6H_4S_2$) using femtosecond lasers that the long-lived triplet state is populated *via* ultrafast intersystem crossing from ligand-to-Ag_{13} core charge transfer state.[131] Unexpectedly, PES on $[M_{25}(PET)_{18}]^-$ (M = Ag, Au) revealed that thermionic emission (TE) of a slow electron dominates over direct photodetachment upon photoirradiation at 266 nm.[128] It was proposed that electronically-excited $[M_{25}(PET)_{18}]^{-}$*, which is embedded in the photodetachment continuum, quickly undergoes internal conversion to form vibrationally excited $[M_{25}(PET)_{18}]^-$ followed by TE leaving internal energy in the remaining neutral $[M_{25}(PET)_{18}]^0$. Protection of the M_{13} core by stiff $M_2(PET)_3$ units may contribute to promoting the IC process of $[M_{25}(PET)_{18}]^{-}$* by retarding the dissociation.

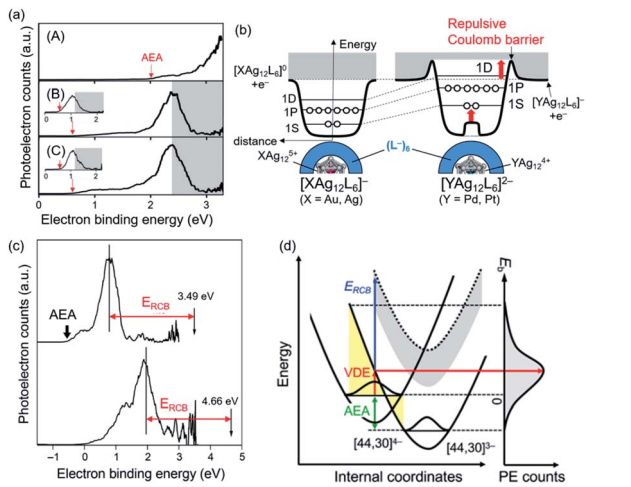

Fig. 13 (a) PE spectra of (A) $[Ag_{25}(2,4\text{-DMBT})_{18}]^-$, (B) $[PtAg_{24}(2,4\text{-DMBT})_{18}]^{2-}$, (C) $[PdAg_{24}(2,4\text{-DMBT})_{18}]^{2-}$ recorded at 355 nm. Insets in panels (B) and (C) are PE spectra recorded at 532 nm. Gray shaded areas in panels (B) and (C) are spectral cutoff regions due to an RCB. (b) Schematic illustration of potentials of $(X@Ag_{12})^{5+}(L^-)_6$ (X = Ag, Au) and $(Y@Ag_{12})^{4+}(L^-)_6$ (Y = Pd, Pt), where L denotes the $Ag_2(2,4\text{-DMBT})_3$ staple unit. d is the distance from an electron and superatoms. (c) PE spectra of $[Ag_{44}(3,4\text{-DFBT})_{30}]^{4-}$ recorded at 355 nm (top) and 266 nm (bottom). (d) Potential energy surfaces of $[Ag_{44}(3,4\text{-DFBT})_{30}]^{4-}$ and $[Ag_{44}(3,4\text{-DFBT})_{30}]^{3-}$ explaining the peak A in panel (c). The yellow hatch indicates the Franck–Condon region. The dotted curve is obtained by upshifting the $[Ag_{44}(3,4\text{-DFBT})_{30}]^{3-}$ curve by E_{RCB}. Adapted with permission from ref. 129 and 130. Copyright 2019 Wiley-VCH and copyright 2020 American Chemistry Society.

Johnson established high-resolution UV-visible absorption spectroscopy at cryogenic temperature in the gas phase.[132–134] Condensation of inert gases (He, N_2) as a tag can freeze the internal motion of the superatoms without noticeable influence on the stable structures. Absorption of UV-visible laser by the tagged superatoms inevitably (with 100% quantum yield) leads to the release of the tags. As a result, the action spectrum of the depletion of the intensity of tagged superatoms corresponds to optical absorption spectra of the ligand-protected superatoms at extremely low temperature. The UV-visible spectrum of $[Au_9(TPP)_8]^{3+}$ exhibits much sharper profiles than that in solution phase thanks to the suppression of thermal broadening (Fig. 14a).[132,133] The spectra at cryogenic temperature can be compared directly with the theoretical spectra (Fig. 14b).[135] It was suggested that hydride and halide affect the electronic structure of $[Au_9(TPP)_8]^{3+}$ in similar ways.[134]

3.2 Condensed phase methods

SCXRD analysis provides the most straightforward and precise structural information of ligand-protected superatoms in the solid state. However, several challenges in structural characterization remain, such as identification of the position of

 This journal is © The Royal Society of Chemistry 2020

Open Access Article. Published on 21 October 2020. Downloaded on 2/15/2026 11:04:09 AM.
This article is licensed under a Creative Commons Attribution-NonCommercial 3.0 Unported Licence.

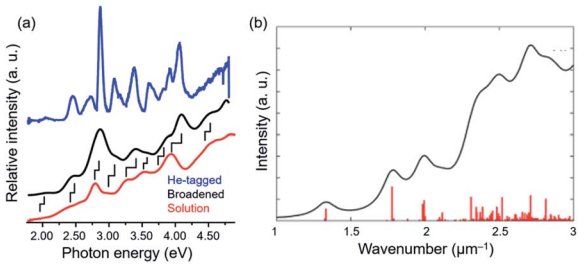

Fig. 14 (a) UV-visible absorption spectra of He-tagged $[Au_9(TPP)_8]^{3+}$ (blue), $[Au_9(TPP)_8]^{3+}(NO_3)_3$ in methanol (red). The black trace is a numerically broadened spectrum of the blue trace. (b) Simulated absorption spectrum of $[Au_9(TPP)_8]^{3+}$. Adapted with permission from ref. 133 and 135. Copyright 2020 American Chemistry Society and copyright 2016 American Chemistry Society.

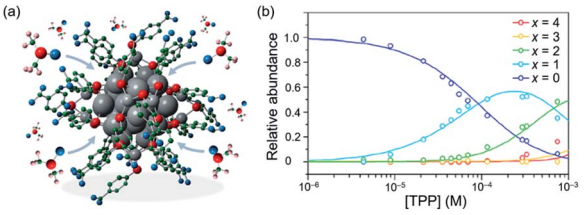

Fig. 15 (a) Scheme of interaction between $Na_4[Ag_{44}(p\text{-MBA})_{30}]$ and DMSO examined by XAS and QM/MM calculation. (b) Plots of relative abundance of $Ag_{29}(BDT)_{12}(TPP)_x$ ($x = 0$–4) in DMF solution as a function of the concentration of TPP. Color code: gray = Ag; red = S; blue = O; green = C, pink = H. Adapted with permission from ref. 145 and 146. Copyright 2020 American Chemistry Society.

doped metal atoms with similar electron densities, structural determination of superatoms that cannot be crystallized, and monitoring the fluctuating system. This section summarizes new approaches to obtain structure information complementary to SCXRD by advanced use of techniques such as XAS, AC(S)TEM, NMR, and PL spectroscopy.

3.2.1 Static structure. Identification of the position of doped metal atoms is sometimes difficult only by SCXRD because it cannot distinguish atoms with similar electron densities. XAS provides detailed structure information such as coordination number and bond length. By taking advantage of element specificity, the locations of the dopants within the bimetallic clusters in a dispersion or in an amorphous solid have been successfully determined.[136] Recently, Maran conducted NMR spectroscopy on isotopically enriched $CdAu_{24}(PET)_{18}$ and concluded by coupling analysis that the Cd dopant is located at the surface of the icosahedral MAu_{12} core regardless of the synthesis methods.[51] The atomic structure of the superatomic cores can be solved by AC(S)TEM on a single superatom, as demonstrated by Palmer, José-Yacamán and Whetten.[137,138] Kornberg successfully constructed the atomic structures of $Au_{68}(m\text{-MBA})_{31,32}$ (m-MBA = 3-SC_6H_4COOH) and $Au_{144}(m\text{-MBA})_{40}$ by ACTEM with the use of a minimal electron dose.[139,140]

3.2.2 Dynamic structure. Ligand-protected superatoms undergo thermal fluctuation under ambient temperature and may be in equilibrium between fully-adsorbed and partially-desorbed states of the ligand layer in solution. An understanding of these dynamic aspects of structural features is essential to establish the correlation between structures and properties. Fluxionality results in polydispersity in atomic structures, making the structural characterization difficult.

Ackerson and Billinge demonstrated by high-energy XRD that $Au_{144}(SR)_{60}$ (R = C_4H_9, C_6H_{13}, $C_{12}H_{25}$, 4-C_6H_4COOH) has a distinct isomer with an fcc core,[141] in addition to that with an icosahedral core identified by SCXRD.[28] However, it was not clear whether they are interconverted with each other or coexist independently. Tsukuda monitored the spatiotemporal change of individual particles of $Au_{144}(PET)_{60}$ by ACTEM and found reversible isomerization between icosahedral and fcc cores without decomposition.[142] Tsukuda and Yamazoe revealed the hierarchy of bond stiffness of Au–Au bonds in $Au_{25}(PET)_{18}$, $Au_{38}(PET)_{24}$, and $Au_{144}(PET)_{60}$ by temperature-dependent extended X-ray absorption fine structure (EXAFS) analysis.[143] It was shown that surface Au–Au bonds of the Au cores are more flexible than those in bulk metals while those distributed along the radial direction are stiffer.

Zhang examined the interaction of solvent and superatoms,[144,145] which is often overlooked due to the difficulty of characterization in solution. A slight change of geometric and electronic structure of $[Ag_{44}(p\text{-MBA})_{30}]^{4-}$ in solution was monitored by XAS.[145] The contraction of the Ag_{32} core and the reduced electron densities of the S atoms suggested that dimethyl sulfoxide (DMSO) and *N*,*N*-dimethylformamide (DMF) directly interact with the $\mathbf{Ag_{32}}$(18e) core (Fig. 15a). These results were supported by quantum mechanics/molecular mechanics (QM/MM) calculations.[145] Mitsui conducted quantitative analysis of the association-dissociation equilibria of TPP in $[Ag_{29}(BDT)_{12}(TPP)_4]^{3-}$ based on PL measurement.[146] The relative abundance of $[Ag_{29}(BDT)_{12}(TPP)_x]^{3-}$ (x = 0–4) as a function of the concentration of TPP added in solution ([TPP]) was determined (Fig. 15b). This optical approach provides a nondestructive method for evaluating the concentrations of superatoms under dynamic equilibrium such as ligand-exchange and metal-exchange reactions.

3.3 Computational methods

Initial geometries for structure prediction by DFT calculation are usually constructed based on the intuition of individual researchers; this approach lacks the completeness, efficiency, and subjectivity. Recently, Kärkkäinen and Häkkinen developed an algorithm based on machine learning to predict the structures of ligand-protected superatoms.[147] After setting the coordinates of metal atoms, a list of possible positions of interface atoms (P or S) is constructed based on the training set consisting of SCXRD data and computational model structures. Then, complete interfacial structures (~10 000 models) are created under a restriction based on simple rules of chemistry related to coordination, atomic distances, and local conformations. Finally, model structures are ranked by a criterion called a combined structural error and optimized to the best model structure after adding the organic part of the ligand layer using molecular mechanics or molecular dynamics. In all studied cases, the best-ranked structures reproduced the metal–ligand

Open Access Article. Published on 21 October 2020. Downloaded on 2/15/2026 11:04:09 AM.
This article is licensed under a Creative Commons Attribution-NonCommercial 3.0 Unported Licence.

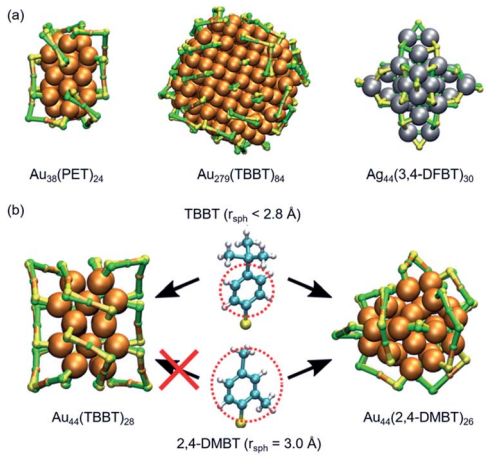

Fig. 16 (a) Comparison of the predicted ligand–metal interface structures (green) and those resolved by SCXRD (yellow). (b) The effect of the size of ligands on the structures. Color code: orange = Au; gray = Ag, green and yellow = S; light blue = C; white = H. Adapted from ref. 147 with permission from Nature Publishing Group, copyright 2019.

interfaces of the crystal structures of a variety of Au/Ag superatoms (Fig. 16a). This method also reproduced the steric effect of ligands in $Au_{44}(TBBT)_{26}$ and $Au_{44}(2,4\text{-}DMBT)_{28}$ (Fig. 16b).

Optimal conditions for the synthesis and crystallization have also been researched based on the experience of individual researchers. Wang demonstrated that deep learning can accelerate the search for synthesis conditions:[148] the conditions for synthesizing $Au_{25}(SR)_{18}$ reported in the literature were successfully predicted from a database containing only 54 results. Application of this approach to other issues requires the establishment of a reliable database which includes both successful and unsuccessful results. Since published papers include only successful cases, joint research between theoretical and experimental chemists is indispensable to expand this area.

4. Summary and prospects

As briefly summarized in the introduction, atomically-precise synthesis and structural determination by X-ray crystallography have deepened our understanding of the correlation between structures and properties of ligand-protected Au/Ag superatoms. The superatom concept provides a unified picture of how the electronic structures are modified or affected by the size, shape and doping. In spite of great progress in the last two decades, there still remain challenges in the synthesis and characterization of the ligand-protected superatoms. Major issues and possible solutions of the synthesis and characterization of Au/Ag superatoms are summarized below.

4.1 Synthesis

Major challenges in the conventional synthesis of superatoms are poor predictability and low yield of the products arising from the stochastic nature of the formation processes. A promising approach includes efficient and selective transformations of well-defined superatoms, such as hydride-mediated growth and doping, seed-mediated growth, and ligand exchange. These transformations will not only achieve the synthesis of desired superatoms on a large (>gram) scale, but also increase the chance of serendipitous discoveries of new superatoms. Another challenge is improvement of robustness for practical application. Recent examples show that N-heterocyclic carbenes are promising candidates for the protecting reagent of Au/Ag superatoms. Large scale synthesis of robust Au/Ag superatoms is a key for the progress of materials science of superatoms as in the case of the development of carbon materials after large-scale production of C_{60} which was originally discovered as magic species by MS.[149] Synthesis of superatomic molecules and ordered assemblies of superatoms will continue to be a challenge for the creation of novel properties and functions by taking advantage of controlled interaction between individual superatoms.

4.2 Characterization

Ligand-protected Au/Ag superatoms have been characterized in depth by various methods conventionally used in chemical analysis. X-ray crystallography is without doubt the most direct and powerful method for determining the atomic structures. However, other experimental methods need to be developed to detect transient species that plays an important role in transformation reactions and to gain intrinsic structural information of the superatoms in an isolated environment. ESI MS makes it possible to detect key species in solution. Laser photoelectron spectroscopy probes the superatomic electronic structures and elucidates the effect of doping and total charge on the electronic structures. Information about the stability and structural motifs will be obtained by applying other gas-phase methods such as collision-induced dissociation MS, ion mobility MS, photodissociation MS and surface-induced dissociation MS. Aberration corrected transmission electron microscopy and X-ray absorption spectroscopy give both static and dynamic structural information of superatoms complementary to SCXRD. Theoretical prediction based on machine learning will not only become a powerful tool for the structural exploration of superatoms, but also release scientists from the tedious screening of synthesis conditions.

As shown in Fig. 3, superatoms are attractive and promising elements having multi-parameters (size, shape, composition) for the control and tuning of their properties. Some future prospects to maximize the potentials of superatoms are described below.

(1) Chemical modifications. Surface modification significantly affects robustness, geometric structures, and properties of superatoms such as HOMO–LUMO gaps, redox properties, circular dichroism, photoluminescence properties, and catalysis. Concerning catalysis of superatoms, the biggest benefit of ligand protection is a possibility that atomically-defined catalytic sites can be realized on superatoms. By protecting with properly designed bulky ligands, there appears a possibility that one can synthesize atomically precise superatoms having an exposed surface owing to inter-ligand steric hinderance and can

 This journal is © The Royal Society of Chemistry 2020

Open Access Article. Published on 21 October 2020. Downloaded on 2/15/2026 11:04:09 AM.
This article is licensed under a Creative Commons Attribution-NonCommercial 3.0 Unported Licence.

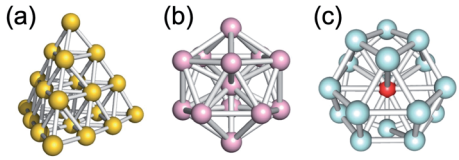

Fig. 17 Proposed structures of superatoms generated in the gas phase: (a) Au_{20}, (b) Al_{13}^-, and (c) $(TM)_1@Si_{16}$. Color code: yellow = Au; pink = Al, light blue = Si; red = TM.

solve the structures by SCXRD. A promising example can be found in CO oxidation catalyzed by $[Au_{22}(Ph_2P(CH_2)_8PPh_2)_6]^0$ (ref. 150) which has 10 unligated Au atoms of the $\mathbf{Au_{22}}$(22e) core.[107] Theoretical study also demonstrated that the exposed sites of $\mathbf{Au_{22}}$(22e) are potentially effective for electrocatalytic hydrogen evolution reaction.[151] This approach will provide molecular-level understanding on the correlation between catalytic performance (activity and selectivity) and structures of the active sites.

Chemical synthesis of $\mathbf{Au_{20}}$(20e) with a tetrahedral pyramid structure (Fig. 17a), which has been the representative magic Au cluster since its discovery,[152] is a long-pursued target. Wang and Wang independently synthesized $\mathbf{Au_{20}}$(16e) using a tetradentate phosphine ligand ($P(C_2H_4PPh_2)_3$).[153,154] However, SCXRD analysis showed that the $\mathbf{Au_{20}}$(16e) core does not have a pyramidal motif, but is composed of an icosahedral Au_{13} and a helical Au_7 motif. Formation of an Au_{41} with a twisted pyramid structure using bulky arenethiols[155] suggests that bulky ligands are possible candidates to stabilize a tetrahedral $\mathbf{Au_{20}}$(20e).

(2) Expansion to other elements. It is known that superatomic concepts can be applicable to cluster systems composed of other than Au and Ag. Schnöckel have synthesized C_5Me_5-protected Al superatoms such as $\mathbf{Al_4}$(8e), $\mathbf{Si@Al_{14}}$(40e), and $\mathbf{Al_{50}}$(138e) by disproportionation of Al(I) produced by vapor deposition and resolved their structures by SCXRD.[156] Magic clusters Al_{13}^- and $(TM)_1@Si_{16}$ (TM = Sc^-, Ti^0, V^+, Y^-, Zr^0, Nb^+, Lu^-, Tb^0, Ho^+, Hf^0, Ta^+) are like holy grails discovered in the history of research on naked metal and inorganic clusters.[32,157] Their electronic shells are closed with the n^* values of 40 and 68, respectively, by setting the A value of eqn (1) to 3, 4 and 4 for Al, TM and Si atoms, respectively. It was proposed that $\mathbf{Al_{13}^-}$(40e) and $\mathbf{(TM)_1@Si_{16}}$(68e) has an icosahedral structure[32] and a caged structure,[157] respectively (Fig. 17b, c). Recently, Yamamoto reported synthesis of $\mathbf{Al_{13}^-}$(40e) encapsulated within dendric poly-phenylazomethine (DPA)[158] by reducing Al(III) coordinated within DPA by benzophenone ketyl radicals. The identification of Al_{13}^- was based on MALDI MS and HAADF STEM observation. High stability of Al_{13}^- in DPA against oxidation agrees with the poor reactivity to O_2 observed in the gas phase.[32] Nakajima achieved large-scale synthesis (100 mg) of polymer-stabilized $\mathbf{Ta^+@Si_{16}}$(68e) and $\mathbf{Ti@Si_{16}}$(68e) using a high-power impulse magnetron sputtering source.[159] Tetrahedral Si cage with Frank–Kasper structure was proposed based on the characterization by NMR, MS, XPS, and Raman spectroscopy. However, their structural determination is still a challenge because they are unstable under aerobic conditions and SCXRD may not be applied. Expansion of the scope to other elements than Au and Ag will open up a new avenue of materials science of superatoms.

The ultimate goal, from our perspective, is to create a new paradigm on a nanoscale based on superatoms, which is located in a different hierarchy from that based on atoms and molecules. The efforts described herein will help to establish the fundamentals of superatoms, such as a periodic table, bonding theories, chemical reaction theories of superatoms, and eventually, the materials chemistry of superatoms.

Conflicts of interest

There are no conflicts to declare.

Acknowledgements

This research was financially supported by a Grant-in-Aid for Scientific Research (JP17H01182, JP20H00370) from the Ministry of Education, Culture, Sports, Science, and Technology (MEXT).

Notes and references

1 W. de Heer, *Rev. Mod. Phys.*, 1993, **65**, 611–676.
2 D. M. P. Mingos, T. Slee and L. Zhenyang, *Chem. Rev.*, 1990, **90**, 383–402.
3 P. Pyykkö, *Chem. Soc. Rev.*, 2008, **37**, 1967–1997.
4 Z. Luo, A. W. Castleman Jr and S. N. Khanna, *Chem. Rev.*, 2016, **116**, 14456–14492.
5 P. Jena and Q. Sun, *Chem. Rev.*, 2018, **118**, 5755–5870.
6 M. McPatrlin, R. Mason and L. Malatesta, *J. Chem. Soc. D*, 1969, 334.
7 K. Konishi, *Struct. Bonding*, 2014, **161**, 49–86.
8 M. Brust, M. Walker, D. Bethell, D. J. Schiffrin and R. Whyman, *J. Chem. Soc., Chem. Commun.*, 1994, 801–802.
9 R. Jin, C. Zeng, M. Zhou and Y. Chen, *Chem. Rev.*, 2016, **116**, 10346–10413.
10 I. Chakraborty and T. Pradeep, *Chem. Rev.*, 2017, **117**, 8208–8271.
11 R. L. Whetten, J. T. Khoury, M. M. Alvarez, S. Murthy, I. Vezmar, Z. L. Wang, P. W. Stephens, C. L. Cleveland, W. D. Luedtke and U. Landman, *Adv. Mater.*, 1996, **8**, 428–433.
12 C. L. Cleveland, U. Landman, T. G. Schaaff, M. N. Shafigullin, P. W. Stephens and R. L. Whetten, *Phys. Rev. Lett.*, 1997, **79**, 1873.
13 S. Chen, R. S. Ingram, M. J. Hostetler, J. J. Pietron, R. W. Murray, T. G. Schaaff, J. T. Khoury, M. M. Alvarez and R. L. Whetten, *Science*, 1998, **280**, 2098–2101.
14 A. C. Templeton, W. P. Wuelfing and R. W. Murray, *Acc. Chem. Res.*, 2000, **33**, 27–36.
15 Y. Negishi, K. Nobusada and T. Tsukuda, *J. Am. Chem. Soc.*, 2005, **127**, 5261–5270.
16 N. K. Chaki, Y. Negishi, H. Tsunoyama, Y. Shichibu and T. Tsukuda, *J. Am. Chem. Soc.*, 2008, **130**, 8608–8610.
17 H. Qian and R. Jin, *Nano Lett.*, 2009, **9**, 4083–4087.

Open Access Article. Published on 21 October 2020. Downloaded on 2/15/2026 11:04:09 AM. This article is licensed under a Creative Commons Attribution-NonCommercial 3.0 Unported Licence.

18 S. Vergara, U. Santiago, C. Kumara, D. Alducin, R. L. Whetten, M. J. Yacamán, A. Dass and A. Ponce, *J. Phys. Chem. C*, 2018, **122**, 26733–26738.
19 I. L. Garzón, C. Rovira, K. Michaelian, M. R. Beltran, P. Ordejon, J. Junquera, D. Sanchez-Portal, E. Artacho and J. M. Soler, *Phys. Rev. Lett.*, 2000, **85**, 5250.
20 H. Häkkinen, M. Walter and H. Grönbeck, *J. Phys. Chem. B*, 2006, **110**, 9927–9931.
21 P. D. Jadzinsky, G. Calero, C. J. Ackerson, D. A. Bushnell and R. D. Kornberg, *Science*, 2007, **318**, 430–433.
22 M. W. Heaven, A. Dass, P. S. White, K. M. Holt and R. W. Murray, *J. Am. Chem. Soc.*, 2008, **130**, 3754–3755.
23 M. Zhu, C. M. Aikens, F. J. Hollander, G. C. Schatz and R. Jin, *J. Am. Chem. Soc.*, 2008, **130**, 5883–5885.
24 H. Quan, W. T. Eckenhoff, Y. Zhu, T. Pintauer and R. Jin, *J. Am. Chem. Soc.*, 2010, **132**, 8280–8281.
25 J. Akola, M. Walter, R. L. Whetten, H. Häkkinen and H. Grönbeck, *J. Am. Chem. Soc.*, 2008, **130**, 3756–3757.
26 O. Lopez-Acevedo, H. Tsunoyama, T. Tsukuda, H. Häkkinen and C. M. Aikens, *J. Am. Chem. Soc.*, 2010, **132**, 8210–8218.
27 O. Lopez-Acevedo, J. Akola, R. L. Whetten, H. Grönbeck and H. Häkkinen, *J. Phys. Chem. C*, 2009, **113**, 5035–5038.
28 N. Yan, N. Xia, L. Liao, M. Zhu, F. Jin, R. Jin and Z. Wu, *Sci. Adv.*, 2018, **4**, eaat7259.
29 R. E. Leuchtner, A. C. Harms and A. W. Castleman Jr, *J. Chem. Phys.*, 1989, **91**, 2753–2754.
30 S. N. Khanna and P. Jena, *Phys. Rev. Lett.*, 1992, **69**, 1664–1667.
31 S. N. Khanna and P. Jena, *Phys. Rev. B: Condens. Matter Mater. Phys.*, 1995, **51**, 13705–13716.
32 D. E. Bergeron, A. W. Castleman Jr, T. Morisato and S. N. Khanna, *Science*, 2004, **304**, 84–87.
33 A. W. Castleman Jr and S. N. Khanna, *J. Phys. Chem. C*, 2009, **113**, 2664–2675.
34 Z. Luo and A. W. Castleman Jr, *Acc. Chem. Res.*, 2014, **47**, 2931–2940.
35 D. A. Tomalia and S. N. Khanna, *Chem. Rev.*, 2016, **116**, 2705–2774.
36 A. C. Reber and S. N. Khanna, *Acc. Chem. Res.*, 2017, **50**, 255–263.
37 W. D. Knight, K. Clemenger, W. A. de Heer, W. A. Saunders, M. Y. Chou and M. L. Cohen, *Phys. Rev. Lett.*, 1984, **52**, 2141–2143.
38 K. J. Taylor, C. L. Pettiette-Hall, O. Cheshnovsky and R. E. Smalley, *J. Chem. Phys.*, 1992, **96**, 3319–3329.
39 M. Walter, J. Akola, O. Lopez-Acevedo, P. D. Jadzinsky, G. Calero, C. J. Ackerson, R. L. Whetten, H. Grönbeck and H. Häkkinen, *Proc. Natl. Acad. Sci. U. S. A.*, 2008, **105**, 9157–9162.
40 H. Häkkinen, *Chem. Soc. Rev.*, 2008, **37**, 1847–1859.
41 T. Omoda, S. Takano and T. Tsukuda, *Small*, 2020, DOI: 10.1002/smll.202001439.
42 D. M. P. Mingos, *Dalton Trans.*, 2015, **44**, 6680–6695.
43 S. B. Zhang, M. L. Cohen and M. Y. Chou, *Phys. Rev. B: Condens. Matter Mater. Phys.*, 1987, **36**, 3455–3458.
44 C. Baladrón and J. A. Alonso, *Phys. B*, 1988, **154**, 73–81.
45 E. Janssens, S. Neukermans and P. Lievens, *Curr. Opin. Solid State Mater. Sci.*, 2004, **8**, 185–193.
46 C. Zeng, Y. Chen, K. Iida, K. Nobusada, K. Kirschbaum, K. J. Lambright and R. Jin, *J. Am. Chem. Soc.*, 2016, **138**, 3950–3953.
47 W. W. Xu, X. C. Zeng and Y. Gao, *Acc. Chem. Res.*, 2018, **51**, 2739–2747.
48 R. Jin, Y. Pei and T. Tsukuda, *Acc. Chem. Res.*, 2019, **52**, 1.
49 S. Takano, H. Hirai, S. Muramatsu and T. Tsukuda, *J. Am. Chem. Soc.*, 2018, **140**, 8380–8383.
50 S. Takano, H. Hirai, S. Muramatsu and T. Tsukuda, *J. Am. Chem. Soc.*, 2018, **140**, 12314–12317.
51 S. Takano, S. Hasegawa, M. Suyama and T. Tsukuda, *Acc. Chem. Res.*, 2018, **51**, 3074–3083.
52 H. Hirai, S. Takano and T. Tsukuda, *ACS Omega*, 2019, **4**, 7070–7075.
53 S. Takano, S. Ito and T. Tsukuda, *J. Am. Chem. Soc.*, 2019, **141**, 15994–16002.
54 Q. Yao, X. Yuan, V. Fung, Y. Yu, D. T. Leong, D.-e. Jiang and J. Xie, *Nat. Commun.*, 2017, **8**, 927.
55 Z. Gan, N. Xia and A. Wu, *Acc. Chem. Res.*, 2018, **51**, 2774–2783.
56 S. Wang, Q. Li, X. Kang and M. Zhu, *Acc. Chem. Res.*, 2018, **51**, 2784–2794.
57 A. Ghosh, O. F. Mohammed and O. M. Bakr, *Acc. Chem. Res.*, 2018, **51**, 3094–3103.
58 S. Hossain, Y. Niihori, L. V. Nair, B. Kumar, W. Kurashige and Y. Negishi, *Acc. Chem. Res.*, 2018, **51**, 3114–3124.
59 W. Fei, S. Antonello, T. Dainese, A. Dolmella, M. Lahtinen, K. Rissanen, A. Venzo and F. Maran, *J. Am. Chem. Soc.*, 2019, **141**, 16033–16045.
60 M. S. Bootharaju, C. P. Joshi, M. R. Parida, O. F. Mohammed and O. M. Bakr, *Angew. Chem., Int. Ed.*, 2015, **128**, 934–938.
61 K. Zheng, V. Fung, X. Yuan, D.-e. Jiang and J. Xie, *J. Am. Chem. Soc.*, 2019, **141**, 18977–18983.
62 K. R. Krishnadas, A. Baksi, A. Ghosh, G. Nararajan, A. Som and T. Pradeep, *Acc. Chem. Res.*, 2017, **50**, 1988–1996.
63 K. R. Krishnadas, A. Baksi, A. Ghosh, G. Natarajan and T. Pradeep, *Nat. Commun.*, 2016, **7**, 13447.
64 M. Suyama, S. Takano, T. Nakamura and T. Tsukuda, *J. Am. Chem. Soc.*, 2019, **141**, 14048–14051.
65 M. R. Narouz, K. M. Osten, P. J. Unsworth, R. W. Y. Man, K. Salorinne, S. Takano, R. Tomihara, S. Kaappa, S. Malola, C.-T. Dinh, J. D. Padmos, K. Ayoo, P. J. Garret, M. Nambo, J. H. Hortoon, E. H. Sargent, H. Häkkinen, T. Tsukuda and C. M. Crudden, *Nat. Chem.*, 2019, **11**, 419–425.
66 X. Meng, Q. Xu, S. Wang and M. Zhu, *Nanoscale*, 2012, **4**, 4161–4165.
67 W. Kurashige, M. Yamaguchi, K. Nobusada and Y. Negishi, *J. Phys. Chem. Lett.*, 2012, **3**, 2649–2652.
68 C. Zeng, Y. Chen, A. Das and R. Jin, *J. Phys. Chem. Lett.*, 2015, **6**, 2976–2986.
69 X. Kang and M. Zhu, *Chem. Mater.*, 2019, **31**, 9939–9969.
70 C. Zeng, C. Liu, Y. Chen, N. Rosi and R. Jin, *J. Am. Chem. Soc.*, 2014, **136**, 11922–11925.

 This journal is © The Royal Society of Chemistry 2020

Open Access Article. Published on 21 October 2020. Downloaded on 2/15/2026 11:04:09 AM.
This article is licensed under a Creative Commons Attribution-NonCommercial 3.0 Unported Licence.

71 C. Zeng, T. Li, A. Das, N. L. Rosi and R. Jin, *J. Am. Chem. Soc.*, 2013, **135**, 10011–10013.
72 C. Zeng, H. Qian, T. Li, G. Li, N. L. Rosi, B. Yoon, R. N. Barnett, R. L. Whetten, U. Landman and R. Jin, *Angew. Chem., Int. Ed.*, 2012, **51**, 13114–13118.
73 M. Rambukwella, L. Sementa, A. Fortunelli and A. Dass, *J. Phys. Chem. C*, 2017, **121**, 14929–14935.
74 C. Zeng, Y. Chen, K. Kirschbaum, K. Appavoo, M. Y. Sfeir and R. Jin, *Sci. Adv.*, 2015, **1**, e1500045.
75 P. R. Nimmala, S. Theivendran, G. Barcaro, L. Sementa, C. Kumara, V. R. Jupally, E. Apra, M. Stener, A. Fortunelli and A. Dass, *J. Phys. Chem. Lett.*, 2015, **6**, 2134–2139.
76 P. R. Nimmala and A. Dass, *J. Am. Chem. Soc.*, 2014, **136**, 17016–17023.
77 E. Khatun, A. Ghosh, D. Ghosh, P. Chakraborty, A. Nag, B. Mondal, S. Chennu and T. Pradeep, *Nanoscale*, 2017, **9**, 8240–8248.
78 A. Dass, T. C. Jones, S. Teivendran, L. Sementa and A. Fortunelli, *J. Phys. Chem. C*, 2017, **121**, 14914–14919.
79 Y. Chen, C. Liu, Q. Tang, C. Zeng, T. Higaki, A. Das, D.-e. Jiang, N. L. Rosi and R. Jin, *J. Am. Chem. Soc.*, 2016, **138**, 1482–1485.
80 M. S. Bootharaju, C. P. Joshi, M. Alhilaly and O. M. Bakr, *Chem. Mater.*, 2016, **28**, 3292–3297.
81 X. Kang, L. Hang, W. Liu, L. Xiong, Y. Pei, Z. Sun, S. Wang, S. Wei and M. Zhu, *Chem. Sci.*, 2019, **10**, 8685–8693.
82 C. M. Crudden, J. H. Horton, I. I. Ebralidze, O. V. Zenkina, A. B. McLean, B. Drevniok, Z. She, H.-B. Kraatz, N. J. Mosey, T. Seki, E. C. Keste, J. D. Leake, A. Rousina-Webb and G. Wu, *Nat. Chem.*, 2014, **6**, 409–414.
83 A. V. Zhukhovitskiy, M. J. MacLeod and J. A. Johnson, *Chem. Rev.*, 2015, **115**, 11503–11532.
84 C. A. Smith, M. R. Narouz, P. A. Lummis, I. Singh, A. Nazemi, C.-H. Li and C. M. Crudden, *Chem. Rev.*, 2019, **119**, 4986–5056.
85 Q. Tang and D.-e. Jiang, *Chem. Mater.*, 2017, **29**, 6908–6915.
86 M. R. Narouz, S. Takano, P. A. Lummis, T. I. Levchenko, A. Nazemi, S. Kaappa, S. Malola, G. Yousefalizadeh, L. A. Calhoun, K. G. Stamplecoskie, H. Häkkinen, T. Tsukuda and C. M. Crudden, *J. Am. Chem. Soc.*, 2019, **141**, 14997–15002.
87 H. Shen, G. Deng, S. Kaapa, T. Tan, Y.-Z. Han, S. Maola, S.-C. Lin, B. K. Teo, H. Häkkinen and N. Zheng, *Angew. Chem., Int. Ed.*, 2019, **58**, 17731–17735.
88 H. Shen, S. Xiang, Z. Xu, C. Liu, X. Li, C. Sun, S. Lin, B. K. Teo and N. Zheng, *Nano Res.*, 2020, **13**, 1908–1911.
89 A. Desireddy, B. E. Conn, J. Guo, B. Yoon, R. N. Barnett, B. N. Monahan, K. Kirschbaum, W. P. Griffith, R. L. Whetten, U. Landman and T. P. Bigioni, *Nature*, 2013, **501**, 399–402.
90 H. Yang, Y. Wang, H. Huang, L. Gell, L. Lehtovaara, S. Maola, H. Häkkinen and N. Zheng, *Nat. Commun.*, 2013, **4**, 2422.
91 B. Bhattarai, I. Chakraborty, B. E. Conn, A. Atnagulov, T. Pradeep and T. P. Bigioni, *J. Phys. Chem. C*, 2017, **121**, 10964–10970.
92 J. Yan, H. Su, H. Yang, C. Hu, S. Maola, S. Lin, B. K. Teo, H. Häkkinen and N. Zheng, *J. Am. Chem. Soc.*, 2016, **138**, 12751–12754.
93 A. Chen, X. Kang, S. Jin, W. Du, S. Wang and M. Zhu, *J. Phys. Chem. Lett.*, 2019, **10**, 6124–6128.
94 M. B. Plutschack, B. Pieber, K. Gilmore and P. H. Seeberger, *Chem. Rev.*, 2017, **117**, 11796–11893.
95 J. Zhang, C. Gong, X. Zeng and J. Xie, *Coord. Chem. Rev.*, 2016, **324**, 39–53.
96 J. A. Darr, J. Zhang, N. M. Makwana and X. Weng, *Chem. Rev.*, 2017, **117**, 1125–11238.
97 L. Cheng, C. Ren, X. Zhang and J. Yang, *Nanoscale*, 2013, **5**, 1475–1478.
98 J. Nishigaki, S. Yamazoe, S. Kohara, A. Fujiwara, W. Kurashige, Y. Negishi and T. Tsukuda, *Chem. Commun.*, 2014, **50**, 839–841.
99 X. Zou, S. Jin, W. Du, Y. Li, S. Wang, P. Li and M. Zhu, *Nanoscale*, 2017, **9**, 16800–16805.
100 Y. Shichibu, Y. Negishi, T. Watanabe, N. K. Chaki, H. Kawaguchi and T. Tsukuda, *J. Phys. Chem. C*, 2007, **111**, 7845–7847.
101 H. Qian, W. Eckenhoff, M. Bie, T. Pintauer and R. Jin, *Inorg. Chem.*, 2011, **50**, 10735–10739.
102 R. Jin, C. Liu, S. Zhao, A. Das, H. Xing, C. Gayathri, Y. Xing, N. L. Rosi, R. R. Gil and R. Jin, *ACS Nano*, 2015, **9**, 8530–8536.
103 Y. Song, F. Fu, J. Zhang, J. Chai, X. Kang, P. Li, S. Li, H. Zhou and M. Zhu, *Angew. Chem., Int. Ed.*, 2015, **54**, 8430–8434.
104 Y. Song, S. Jin, X. Kang, J. Xiang, H. Deng, H. Yu and M. Zhu, *Chem. Mater.*, 2016, **28**, 2609–2617.
105 K. Zheng, J. Zhang, D. Zhao, Y. Yang, Z. Li and G. Li, *Nano Res.*, 2019, **12**, 501–507.
106 T.-H. Chiu, J.-H. Liao, F. Gam, I. Chantrenne, S. Kahlal, J.-Y. Saillard and C. W. Liu, *J. Am. Chem. Soc.*, 2019, **141**, 12957–12961.
107 J. Chen, Q.-F. Zhang, T. A. Bonaccorso, P. G. Williard and L.-S. Wang, *J. Am. Chem. Soc.*, 2014, **136**, 92–95.
108 A. Muñoz-Castro, *Phys. Chem. Chem. Phys.*, 2020, **22**, 1422–1426.
109 T. Dianese, S. Antonello, S. Bogialli, W. Fei, A. Venzo and F. Maran, *ACS Nano*, 2018, **12**, 7057–7066.
110 E. Ito, S. Takano, T. Nakamura and T. Tsukuda, *Angew. Chem., Int. Ed.*, 2020, DOI: 10.1002/anie.202010342.
111 S.-F. Yuan, J.-J. Li, Z.-J. Guan, Z. Lei and Q.-M. Wang, *Chem. Commun.*, 2020, **56**, 7037–7040.
112 A. Ebina, S. Hossain, S. Ozaki, S. Kato, T. Kawawaki and Y. Negishi, *Nanomaterials*, 2020, **10**, 1105.
113 M. D. Nardi, S. Antonello, D.-e. Jiang, F. Pan, K. Rissanen, M. Ruzzi, A. Venzo, A. Zoleo and F. Maran, *ACS Nano*, 2014, **8**, 8505–8512.
114 P. Yuan, R. Zhang, E. Selenius, P. Ruan, Y. Yao, Z. Zhou, S. Maola, H. Häkkinen, B. K. Teo, Y. Cao and N. Zheng, *Nat. Commun.*, 2020, **11**, 2229.
115 Q. Li, J. C. Russell, T.-Y. Luo, X. Roy, N. L. Rosi, Y. Zhu and R. Jin, *Nat. Commun.*, 2018, **9**, 3871.

Open Access Article. Published on 21 October 2020. Downloaded on 2/15/2026 11:04:09 AM. This article is licensed under a Creative Commons Attribution-NonCommercial 3.0 Unported Licence.

116 Z.-Y. Wang, M.-Q. Wang, Y.-L. Li, P. Luo, T.-T. Jia, R.-W. Huang, S.-Q. Zang and T. C. W. Mak, *J. Am. Chem. Soc.*, 2018, **140**, 1069–1076.
117 S. Chen, W. Du, C. Qin, D. Liu, L. Tang, Y. Liu, S. Wang and M. Zhu, *Angew. Chem., Int. Ed.*, 2020, **59**, 7542–7547.
118 G. E. Johnson and J. Laskin, *Analyst*, 2016, **141**, 3573–3589.
119 K. Hirata, R. Tomihara, K. Kim, K. Koyasu and T. Tsukuda, *Phys. Chem. Chem. Phys.*, 2019, **21**, 17463–17474.
120 P. Chakraborty and T. Pradeep, *NPG Asia Mater.*, 2019, **11**, 48.
121 T. Chen, Q. Yao, R. R. Nasaruddin and J. Xie, *Angew. Chem., Int. Ed.*, 2019, **58**, 11967–11977.
122 K. Koyasu, K. Hirata and T. Tsukuda, in *Physical Chemistry of Cold Gas-Phase Functional Molecules and Clusters*, ed. T. Ebata and M. Fujii, Springer, 2019, pp. 223–253.
123 Q. Yao, T. Chen, X. Yuan and J. Xie, *Acc. Chem. Res.*, 2018, **51**, 1338–1348.
124 T. Chen, V. Fung, Q. Yao, Z. Luo, D. E. Jiang and J. Xie, *J. Am. Chem. Soc.*, 2018, **140**, 11370–11377.
125 A. Ghosh, M. Bodiuzzaman, A. Nag, M. Jash, A. Baksi and T. Pradeep, *ACS Nano*, 2017, **11**, 11145–11151.
126 S. Ito, K. Koyasu, S. Takano and T. Tsukuda, *J. Phys. Chem. C*, 2020, **124**, 19119–19125.
127 K. Hirata, K. Yamashita, S. Muramatsu, S. Takano, K. Ohshimo, T. Azuma, R. Nakanishi, T. Nagata, S. Yamazoe, K. Koyasu and T. Tsukuda, *Nanoscale*, 2017, **9**, 13409–13412.
128 K. Hirata, K. Kim, K. Nakamura, H. Kitazawa, S. Hayashi, K. Koyasu and T. Tsukuda, *J. Phys. Chem. C*, 2019, **123**, 13174–13179.
129 K. Kim, K. Hirata, K. Nakamura, H. Kitazawa, S. Hayashi, K. Koyasu and T. Tsukuda, *Angew. Chem., Int. Ed.*, 2019, **58**, 11637–11641.
130 Y. Tasaka, K. Nakamura, S. Malola, K. Hirata, K. Kim, K. Koyasu, H. Häkkinen and T. Tsukuda, *J. Phys. Chem. Lett.*, 2020, **11**, 3069–3074.
131 A. P. Veenstra, L. Monzel, A. Baksi, J. Czekner, S. Lebedkin, E. K. Schneider, T. Pradeep, A. N. Unterreiner and M. M. Kappes, *J. Phys. Chem. Lett.*, 2020, **11**, 2675–2681.
132 A. Cirri, H. Morales Hernández, C. Kmiotek and C. J. Johnson, *Angew. Chem., Int. Ed.*, 2019, **58**, 13818–13822.
133 A. Cirri, H. M. Hernández and C. J. Johnson, *J. Phys. Chem. A*, 2020, **124**, 1467–1479.
134 A. Cirri, H. M. Hernández and C. J. Johnson, *Chem. Commun.*, 2020, **56**, 1283–1285.
135 N. V Karimova and C. M. Aikens, *J. Phys. Chem. A*, 2016, **120**, 9625–9635.
136 S. Yamazoe and T. Tsukuda, *Bull. Chem. Soc. Jpn.*, 2019, **92**, 193–204.
137 Z. W. Wang, O. Toikkanen, B. M. Quinn and R. E. Palmer, *Small*, 2011, **7**, 1542–1545.
138 D. Bahena, N. Bhattarai, U. Santiago, A. Tlahuice, A. Ponce, S. B. H. Bach, B. Yoon, R. L. Whetten, U. Landman and M. José-Yacamán, *J. Phys. Chem. Lett.*, 2013, **4**, 975–981.
139 M. Azubel, J. Koivisto, S. Malola, D. Bushnell, G. L. Hura, A. L. Koh, H. Tsunoyama, T. Tsukuda, M. Pettersson, H. Häkkinen and R. D. Kornberg, *Science*, 2014, **345**, 909–912.
140 M. Azubel, A. L. Koh, K. Koyasu, T. Tsukuda and R. D. Kornberg, *ACS Nano*, 2017, **11**, 11866–11871.
141 K. M. Ø. Jensen, P. Juhas, M. A. Tofanelli, C. L. Heinecke, G. Vaughan, C. J. Ackerson and S. J. L. Billinge, *Nat. Commun.*, 2016, **7**, 11859.
142 R. Takahata, S. Yamazoe, Y. Maehara, K. Yamazaki, S. Takano, W. Kurashige, Y. Negishi, K. Gohara and T. Tsukuda, *J. Phys. Chem. C*, 2020, **124**, 6907–6912.
143 S. Yamazoe, S. Takano, W. Kurashige, T. Yokoyama, K. Nitta, Y. Negishi and T. Tsukuda, *Nat. Commun.*, 2016, **7**, 10414.
144 D. M. Chevrier, L. Raich, C. Rovira, A. Das, Z. Luo, Q. Yao, A. Chatt, J. Xie, R. Jin, J. Akola and P. Zhang, *J. Am. Chem. Soc.*, 2018, **140**, 15430–15436.
145 D. M. Chevrier, B. E. Conn, B. Li, D. E. Jiang, T. P. Bigioni, A. Chatt and P. Zhang, *ACS Nano*, 2020, **14**, 8433–8441.
146 Y. Niihori, N. Takahashi and M. Mitsui, *J. Phys. Chem. C*, 2020, **124**, 5880–5886.
147 S. Malola, P. Nieminen, A. Pihlajamäki, J. Hämäläinen, T. Kärkkäinen and H. Häkkinen, *Nat. Commun.*, 2019, **10**, 3973.
148 J. Li, T. Chen, K. Lim, L. Chen, S. A. Khan, J. Xie and X. Wang, *Adv. Intell. Syst.*, 2019, **1**, 1900029.
149 H. W. Kroto, J. R. Heath, S. C. O'Brien, R. F. Curl and R. E. Smally, *Nature*, 1985, **318**, 162–163.
150 Z. Wu, G. Hu, D.-e. Jiang, D. R. Mullins, Q.-F. Zhang, L. F. Allard Jr, L.-S. Wang and S. H. Overbury, *Nano Lett.*, 2016, **16**, 6560–6567.
151 G. Hu, Z. Wu and D.-e. Jiang, *J. Mater. Chem. A*, 2018, **6**, 7532–7537.
152 J. Li, H.-J. Zhai and L.-S. Wang, *Science*, 2003, **299**, 864–867.
153 X.-K. Wan, S.-F. Yuan, Z.-W. Lin and Q.-M. Wang, *Angew. Chem., Int. Ed.*, 2014, **53**, 2923–2926.
154 J. Chen, Q.-F. Zhang, P. G. Williard and L.-S. Wang, *Inorg. Chem.*, 2014, **53**, 3932–3934.
155 J. Nishigaki, R. Tsunoyama, H. Tsunoyama, N. Ichikuni, S. Yamazoe, Y. Negishi, M. Ito, T. Matsuo, K. Tamao and T. Tsukuda, *J. Am. Chem. Soc.*, 2012, **134**, 14295–14297.
156 H. Schnöckel, *Chem. Rev.*, 2010, **110**, 4125–4163.
157 K. Koyasu, M. Akutsu, M. Mitsui and A. Nakajima, *J. Am. Chem. Soc.*, 2005, **127**, 4998–4999.
158 T. Kambe, N. Haruta, T. Imaoka and K. Yamamoto, *Nat. Commun.*, 2017, **8**, 2046.
159 H. Tsunoyama, H. Akatsuka, M. Shibuta, T. Iwasa, Y. Mizuhata, N. Tokitoh and A. Nakajima, *J. Phys. Chem. C*, 2017, **121**, 20507–20516.

 This journal is © The Royal Society of Chemistry 2020